



# 1 Retrieval and Validation of Total Seasonal Liquid Water Amounts in 2 the Percolation Zone of Greenland Ice Sheet Using L-band 3 Radiometry

4 Alamgir Hossan<sup>1</sup>, Andreas Colliander<sup>1</sup>, Baptiste Vandecrux<sup>2</sup>, Nicole-Jeanne Schlegel<sup>3</sup>, Joel Harper<sup>4</sup>,  
5 Shawn Marshall<sup>5</sup>, Julie Z Miller<sup>6</sup>

6  
7 <sup>1</sup>Jet Propulsion Laboratory, California Institute of Technology

8 <sup>2</sup>Geological Survey of Denmark and Greenland

9 <sup>3</sup>NOAA/OAR Geophysical Fluid Dynamics Laboratory (GFDL)

10 <sup>4</sup>Department of Geosciences, University of Montana

11 <sup>5</sup>Department of Geography, University of Calgary

12 <sup>6</sup>Cooperative Institute for Research in Environmental Sciences, University of Colorado Boulder

13

14 Correspondence to: Alamgir Hossan ([alamgir.hossan@jpl.nasa.gov](mailto:alamgir.hossan@jpl.nasa.gov)) and Andreas Colliander  
15 ([andreas.colliander@jpl.nasa.gov](mailto:andreas.colliander@jpl.nasa.gov))

16 **Abstract.** Quantifying the total liquid water amounts (LWA) in the Greenland ice sheet (GrIS) is critical for understanding  
17 GrIS firn processes, mass balance, and global sea-level rise. Although satellite microwave observations are very sensitive to  
18 ice sheet melt and thus can provide a way of monitoring the ice sheet melt globally, estimating total LWA, especially the sub-  
19 surface LWA, remains a challenge. Here, we present a microwave retrieval of LWA over Greenland using enhanced resolution  
20 L-band brightness temperature (TB) data products from the NASA Soil Moisture Active Passive (SMAP) satellite for the  
21 2015-2023 period. L-band signals receive emission contributions deep in the ice sheet and are sensitive to the liquid water  
22 content (LWC) in the firn column. Therefore, they can estimate the surface-to-subsurface LWA, unlike higher frequency  
23 signals (e.g., 18 and 37 GHz bands), which are limited to the top few centimeters of the surface snow during the melt. We used  
24 vertically polarized TB (V-pol TB) with empirically derived thresholds to detect liquid water and identify distinct ice sheet  
25 zones. A forward model based on radiative transfer in the ice sheet was used to simulate TB. The simulated TB was then used  
26 in an inversion algorithm to estimate LWA. Finally, the retrievals were compared with the LWA obtained from two sources.  
27 The first source was a locally calibrated ice sheet energy and mass balance (EMB) model, which was forced by *in situ*  
28 measurements from six automatic weather stations (AWS) of the Programme for Monitoring of the Greenland Ice Sheet  
29 (PROMICE) and Greenland Climate Network (GC-Net) located in the percolation zone of the GrIS. The second source was  
30 the corresponding LWA obtained from the Glacier Energy and Mass Balance (GEMB) model within the National Aeronautics  
31 and Space Administration's (NASA) Ice-sheet and Sea-Level System Model (ISSM). The retrievals show generally good



32 agreement with both the references, demonstrating the potential for advancing our understanding of ice sheet physical  
33 processes to better project Greenland's contribution to the global sea level rise in response to the warming climate.

## 34 **1 Introduction**

35 Continuous mass loss of the Greenland Ice Sheet (GrIS) has been a significant concern in the context of climate change and  
36 associated sea level rise (Khan et al., 2015; Mouginit et al., 2019; Otosaka et al., 2023; Shepherd et al., 2020). Greenland has  
37 lost about 330 billion tons of mass, equivalent to around 1 mm global sea level rise, per year on average for the last two decades  
38 (Greene et al., 2024; Khan et al., 2022). This will likely accelerate in the coming decades, even with the most optimistic  
39 warming scenario.

40 Mass loss occurs through surface melt and the subsequent runoff of meltwater towards the ice sheet margin and solid  
41 ice discharge (calving) at marine-terminating outlet glacier termini. While meltwater runoff has been the dominant contributor  
42 to mass loss in Greenland, both have increased in the last few decades (Van Den Broeke et al., 2016; Greene et al., 2024;  
43 Mouginit et al., 2019; Vandecrux et al., 2023a). In the ablation area, the winter snowpack is melted out every summer and the  
44 meltwater enter an efficient drainage network of streams and lakes toward the margin (Smith et al., 2017). Higher up on the  
45 ice sheet, in the accumulation area, there is less melt, and a porous snow layer accumulated over the years, called firn, leads to  
46 the percolation and refreezing of surface melt, buffering additional sea level rise (Harper et al., 2012; Samimi et al., 2020).  
47 However, with intense and frequent melt events, thick ice layers, called ice slabs, are formed from meltwater refreezing,  
48 impeding vertical percolation of meltwater and promoting horizontal runoff (Culberg et al., 2021; Jullien et al., 2023;  
49 MacFerrin et al., 2019; Miller et al., 2022b, 2020b; Tedstone and Machguth, 2022). Increased refreezing resulted in a loss of  
50 approximately 5% of GrIS firn air content (FAC) between 1996 and 2019 (Medley et al., 2022). These effects gradually  
51 diminish the ice sheet's inherent capability to retain meltwater and buffer sea level rise (Harper et al., 2012; Mikkelsen et al.,  
52 2016; Vandecrux et al., 2019).

53 Furthermore, increased melting contributes to forming supraglacial, englacial, and subglacial meltwater features (e.g.,  
54 lakes, rivers, slush, crevasses, moulins, and firn aquifers, etc.) that can augment dynamical discharge and calving losses by  
55 lubricating the basal sliding surface and accelerating the flow of outlet glaciers (Hoffman et al., 2011; Schoof, 2010; Sundal  
56 et al., 2011; Zwally et al., 2002). Therefore, meltwater not only contributes to sea-level rising through direct runoff, but it can  
57 also alter the physical structure that governs the dynamics and evolution of the ice sheet. Hence, quantification of total surface  
58 and subsurface liquid water is essential to understand ice sheet response to climate changes and project sea level rise accurately.

59 Surface melt and liquid water amount (LWA) can be estimated with various techniques. *In situ* AWS networks  
60 provide meteorological observations (Fausto et al., 2021), which can drive surface energy and mass balance (EMB) models to  
61 derive surface melt and LWA. Other *in situ* measurements such as upward-looking radar (Heilig et al., 2018) or time domain  
62 resistivity probes (Samimi et al., 2021) can also be used to measure LWA at a given site. Due to logistical constraints, these  
63 point observations have a limited spatial and temporal coverage.



64 Regional climate models (RCM) are primarily used to estimate ice sheet-wide LWA, surface mass balance (SMB),  
65 and their changes (Fettweis et al., 2020). The results of RCMs are difficult to validate on the scale of the ice sheet, given the  
66 scarcity of *in situ* data to constrain and calibrate these models. Moreover, diversity exists in representation of the surface and  
67 sub-surface firm processes among RCMs, leading to significant uncertainties in LWA estimates and their temporal and spatial  
68 variabilities (Fettweis et al., 2020; Thompson-Munson et al., 2023; Vandecrux et al., 2020; Verjans et al., 2019).

69 Satellite-based observations, especially microwave sensors, are very sensitive to ice sheet melting, manifested by  
70 large changes in dielectric constant with liquid water and can provide global coverage in day-night and all-weather conditions  
71 (Abdalati and Steffen, 1997; Mote and Anderson, 1995; Picard et al., 2022; Tedesco, 2007; Tedesco et al., 2007; Zwally and  
72 Fiegles, 1994). Accordingly, both active (radars) and passive sensors (radiometers) have been used to monitor surface melting  
73 across Greenland and Antarctica ice sheets (Abdalati and Steffen, 1995, 2001; Hall et al., 2009; Mote, 2007; Nghiem et al.,  
74 2001; Tedesco, 2007; Wismann, 2000; Zwally and Fiegles, 1994). However, these conventional approaches applying high-  
75 frequency bands (i.e., 18 and 36 GHz) from the legacy and operational radiometers (Abdalati and Steffen, 1997; Ashcraft and  
76 Long, 2006; Colosio et al., 2021; Fettweis et al., 2007, 2011; Tedesco, 2007, 2009; Tedesco et al., 2007; Zwally and Fiegles,  
77 1994) can only track the surface and near-surface binary melt status, not the meltwater propagation into the deeper layers  
78 because of their limited penetration depth and sensitivity to LWC (Colliander et al., 2022a, b, 2023; Mousavi et al., 2022). The  
79 emergence of L-band (1 - 2 GHz) radiometry, marked by the launch of ESA's Soil Moisture and Ocean Salinity (SMOS)  
80 mission (November 2009 - present) and the collaborative effort between NASA and Argentina's space agency CONAE in the  
81 Aquarius mission (October 2011 - June 2015), followed by NASA's Soil Moisture Active Passive (SMAP) mission (March  
82 2015 - present), has opened up the possibilities for monitoring ice sheet meltwater at greater depths. L-band signals can  
83 penetrate deeper and provide a more accurate estimate of sub-surface liquid water (Colliander et al., 2022b; Miller et al., 2020a,  
84 2022a, b; Mousavi et al., 2022). Nevertheless, only a few attempts have been made to quantify the amount of liquid water  
85 (Colliander et al., 2022a; Houtz et al., 2019, 2021; Mousavi et al., 2021; Schwank and Naderpour, 2018). In this paper, we use  
86 multi-year L-band observations from SMAP to quantify the LWA on the GrIS and examine their spatial and temporal  
87 variability.

## 88 **2 Methods**

### 89 **2.1 SMAP L-band Enhanced Resolution Brightness Temperatures**

90 SMAP was launched on January 31, 2015, and has been operational since March 31, 2015 (Entekhabi et al., 2010). It was  
91 placed in a 685-km altitude and 98.1° inclination sun-synchronous polar orbit with 6 AM/6 PM equator-crossing. It carries a  
92 conically scanning radiometer operating in 1.41 GHz (L-band) with a constant incidence angle of 40° that results 1000-km  
93 wide swath giving twice daily coverage of GrIS. It measures brightness temperature (TB) in fully polarimetric mode giving  
94 the horizontal and vertical polarizations, as well as the 3rd and 4th Stokes parameters with native 38-km spatial resolution.



95 The radiometric precision of the SMAP radiometer is within 0.5 K (Chaubell et al., 2018, 2020; Piepmeier et al., 2017). For  
96 Jun 20 – July 23, 2019, and Aug 6 - Oct 16, 2022, SMAP does not have results because of an operational outage of the satellite.

97 Here, we used SMAP L-band enhanced-resolution TB products generated using the radiometer form of the  
98 Scatterometer Image Reconstruction (rSIR) algorithm and projected on the EASE-2 3.125 km grid (Brodzik et al., 2021; Long  
99 et al., 2019). The rSIR algorithm leverages the measurement response function (MRF) of each observation and combines the  
100 overlapping MRFs to reconstruct enhanced-resolution TB images. The effective resolution of SMAP enhanced-resolution TB  
101 products posted on a 3.125 km grid is ~30 km compared to the 36 km effective resolution of the SMAP original data products  
102 (Long et al., 2023). The data product provides two TB images daily – the morning and evening facilitating the resolution of  
103 diurnal variability. The spatial oversampling and resolution enhancement enables an improved characterization of spatial  
104 heterogeneity (Long et al., 2023). The land–ocean mask used to locate the ice sheet edge comes from PROMICE (Citterio and  
105 Ahlstrøm, 2013).

## 106 **2.2 Microwave Radiometric Response of GrIS**

### 107 **2.2.1 Theoretical Background**

108 Microwave radiometers measure the naturally emitted thermal radiation, called the brightness temperature (TB), by the firm as  
109 observed in the microwave portion of the electromagnetic spectrum. It is related to the emissivity  $e$  and the effective physical  
110 temperature  $T_{phy}$  of snow/firm/ice media for a given frequency  $f$ , polarization  $p$ , and incidence angle  $\theta$ . If firm were vertically  
111 homogeneous or isothermal, the TB could be found according to Rayleigh-Jeans approximation (Ulaby and Long, 2014):

$$112 T_B(f, p, \theta) = e T_{phy} \quad (1)$$

113 However, firm is not a vertically homogenous medium. Both the emissivity and temperature vary with depth. As a  
114 result, the TB is given by a depth-integrated product of physical temperature and emissivity, weighted by the emissive,  
115 absorptive, and scattering properties of the snow/firm/ice layers (Jay Zwally, 1977) which is strongly dependent on the  
116 frequency of observation.

117 To account for the depth dependencies of snow and ice properties, firm is considered as a complex multilayer dense  
118 medium. For each layer, an effective physical temperature and permittivity is determined from firm absorptive and scattering  
119 properties. Then the microwave emission and its propagation are typically modeled using equation of radiative transfer (RT).  
120 Considering firm as a stack of N layers consisting of isotropic and homogeneous material in each layer, the RT equation can  
121 be given as (Jin, 1994, 1997; Picard et al., 2013; Tsang et al., 2000):

$$122 \cos \theta \frac{d}{dz} \mathbf{T}_B(z, \theta, \phi) = \kappa_a \mathbf{T}(z) \mathbf{I} - \kappa_e \mathbf{T}_B(z, \theta, \phi) + \int_0^{\frac{\pi}{2}} \int_0^{2\pi} \sin \theta' d\theta' d\phi' \mathbf{P}(\theta, \phi, \theta', \phi') \mathbf{T}_B(z, \theta', \phi') \quad (2)$$

123 Here,  $\mathbf{T}_B(z, \theta, \phi)$  denotes the vertically and horizontally polarized brightness temperatures at depth  $z$  propagating along a  
124 direction characterized by  $\theta$  (zenith angle) and  $\phi$  (azimuth angle).  $\kappa_e$ ,  $\kappa_a$ , and  $\kappa_s$  are the extinction, absorption, and scattering



125 coefficients, respectively, representing medium properties. For an isotropic medium, the extinction coefficient can be described  
126 as,  $\kappa_e = \kappa_a + \kappa_s$ .  $\theta'$  and  $\phi'$  are slant angles and  $\mathbf{P}$  is bistatic scattering phase function.  $\mathbf{T}(z)$  is the physical temperature of  
127 snow at depth  $z$ , and  $\mathbf{I}$  is a unit vector. Thus, the first term on the right-hand side of Eq. 2 represents the microwave emission  
128 ( $T_B$ ) of snow/fir/ice from depth  $z$ , and the second term denotes the extinction (attenuation) of the emission due to absorption  
129 and scattering. The third term represents the sum of total scattered emission in the direction of the receiver (as specified by  $\theta$   
130 and  $\phi$ ). Eq. 2 is solved analytically or numerically subject to boundary conditions at each layer interface and at the top and  
131 bottom of the medium

132 The extinction coefficient,  $\kappa_e$  is function of the effective dielectric constant of the layer and frequency of the  
133 observation. Thus, the overall TB is given by the depth-integrated profiles of the effective physical temperature and dielectric  
134 constant of each layer. So, penetration depth plays a key role in determining the variability of TB, especially in low-frequency  
135 bands. For a low-loss media like firn, the penetration depth can be approximated as (Elachi and Zyl, 2021):

$$136 \quad \delta = \frac{c\sqrt{\epsilon'}}{2\pi f \epsilon''} \quad (3)$$

137 where  $c$  is the speed of light and,  $\epsilon'$  and  $\epsilon''$  are the real and imaginary parts of the dielectric constant of the firn. As shown,  $\delta$   
138 is inversely proportional to both,  $f$  and  $\epsilon''$ . L-band signal thus penetrates a significantly thicker layer than the higher frequency,  
139 like Ka-band signal. Liquid water markedly increases  $\epsilon''$  (compared to  $\sqrt{\epsilon'}$ ), decreasing the penetration depth for any frequency.

140 There are two types of scattering processes in the snow/firn medium affecting the propagation: surface scattering and  
141 volume scattering. The relative size of the scatterers compared to the wavelength determines the degree and types of scattering.  
142 For high frequency bands ( $>10\text{GHz}$ ), the impact of volume scattering is critical because the fractional volume of scatterers  
143 (snow/firn) is significant. This is why the high-frequency signals interact more with fresh snow, grain size, and roughness at  
144 the surface. Low-frequency signals ( $<10\text{GHz}$ ) are relatively insensitive to volume scattering from snow grains because the size  
145 of the scatterers is much smaller than the wavelength. Surface scattering occurs due to surface irregularities at the interface  
146 between layers of different dielectric constants, affecting all the frequencies when present. Horizontal and vertical ice layers  
147 (strata) are formed at various depths in the firn primarily from the refreezing of seasonal snow melts. Over time, older ice  
148 layers move downward due to the snow accumulation while new ice layers are formed for subsequent melts at the top layers,  
149 creating a complex set of stratigraphy and significantly influencing the L-band signals from the deeper layers. Therefore, L-  
150 band TB is determined by the subsurface temperature, stratigraphy, and LWA.

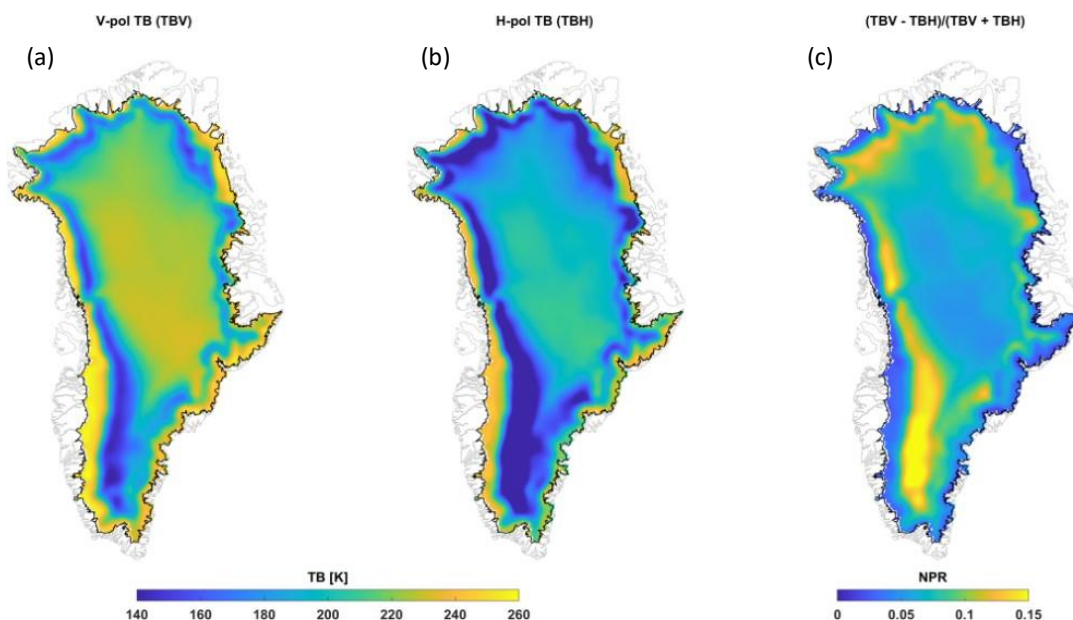
### 151 2.2.2 Frozen Season Response

152 L-band TB exhibit some distinct spatial features over GrIS during a frozen season. Along a typical west-east transect, TB is  
153 the highest in the ablation zone, then it gradually decreases to its lowest value in the percolation zone, followed by a gradual  
154 increase towards a moderate value in the upper accumulation zone. A mirror image is seen on the eastern side of the ice sheet.  
155 The spatial features of H-pol TB are similar to V-pol TB, but it is more affected by sub-surface layering. This is illustrated in



156 Figure 1 with V- and H-pol mean frozen season TBs and their normalized polarization ratio (NPR, defined as  $NPR = (TBV -$   
157  $TBH)/(TBV + TBH)$ ). The ablation zone is characterized by exposed glacial ice with a high density and internal temperature  
158 than those of the ice sheet towards Greenland's interior. It is soaked and swept by a large amount of meltwater every year.  
159 During the frozen season, the L-band emission has a high effective emissivity, radiating the warmer physical temperature of  
160 the deeper layers. In the percolation zone, on the other hand, moderate, but varying melt occurs almost each or every few years  
161 that percolates down and refreezes at different depths forming discrete ice layers and ice pipes, causing substantial scattering  
162 of mean TB (Jezek et al., 2018). High NPR values highlight the area with dense ice layers (strata). The upper accumulation  
163 zone experiences light or no melt but accumulates snow, resulting in less density variation compared to the percolation zone.  
164 For detecting melt and quantifying LWA, we used vertically polarized TB (V-pol TB) considering its lower sensitivity to sub  
165 surface stratigraphy.

166



167

168 **Figure 1: L-band radiometric response of GrIS during frozen season. Vertically polarized TB (a), horizontally polarized TB (b)**  
169 **averaged over Jan 1 – Apr 7<sup>th</sup>, 2015 – 2023, and their normalized polarization difference (c).**

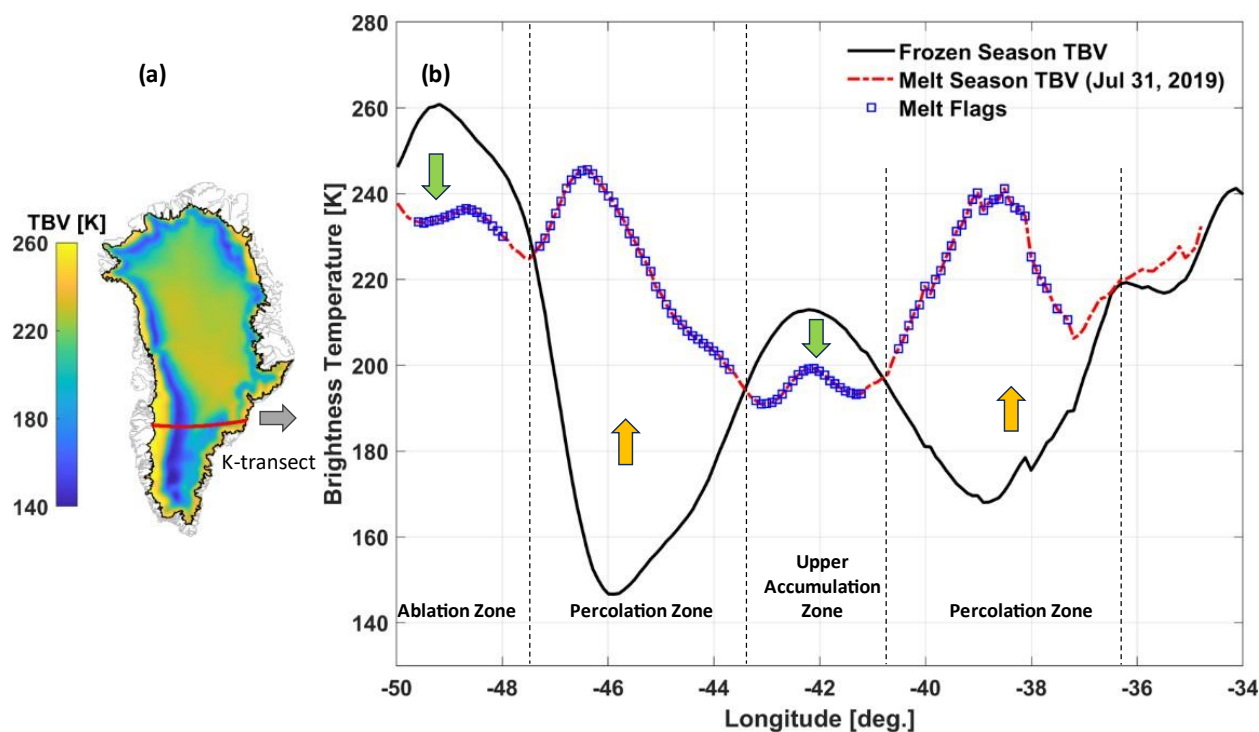
### 170 2.2.3 Melt Season Response

171 During summer season in presence of melt, the L-band TB generally decreases in the ablation and upper accumulation zones  
172 compared to the frozen season, while it increases significantly in the percolation zone. Fig. 2 illustrates this for a sample  
173 summer day (Jul 31, 2019) when melt was detected across the K-transect (~ 67° constant latitude; see the red line in Figure  
174 2a). The melt flags (square symbols over dashed line) specify the TB samples for which melt was detected (Sec. 3.2). The



175 presence of LWC in the snow and firn increases the absorption and emission in turn (Mote and Anderson, 1995). However, at  
 176 the lower elevation around the ablation zone, the TB decreases from its very high level (~260 K) as the LWC of the seasonal  
 177 snow layer increases. This is because, when the LWC in the snow layer exceeds a threshold, snow becomes saturated and it  
 178 creates a reflective boundary at the ice and snow interface, suppressing the emission from the ice layer and resulting in overall  
 179 lower TB. This is caused by intense melting common in the ablation zone (Figure 2b). The percolation zone experiences  
 180 moderate melt, making the snow and firn highly absorptive during melt season. As a result, the TB gradually increases from  
 181 its winter references (Figure 2b), making the L-band sensitive to the total amounts of melt. In the upper accumulation zone,  
 182 melt seldom occurs. But when it occurs, it may percolate and refreezes quickly in the colder snow creating ice layers that cause  
 183 reflection, reducing L-band TB signals.

184



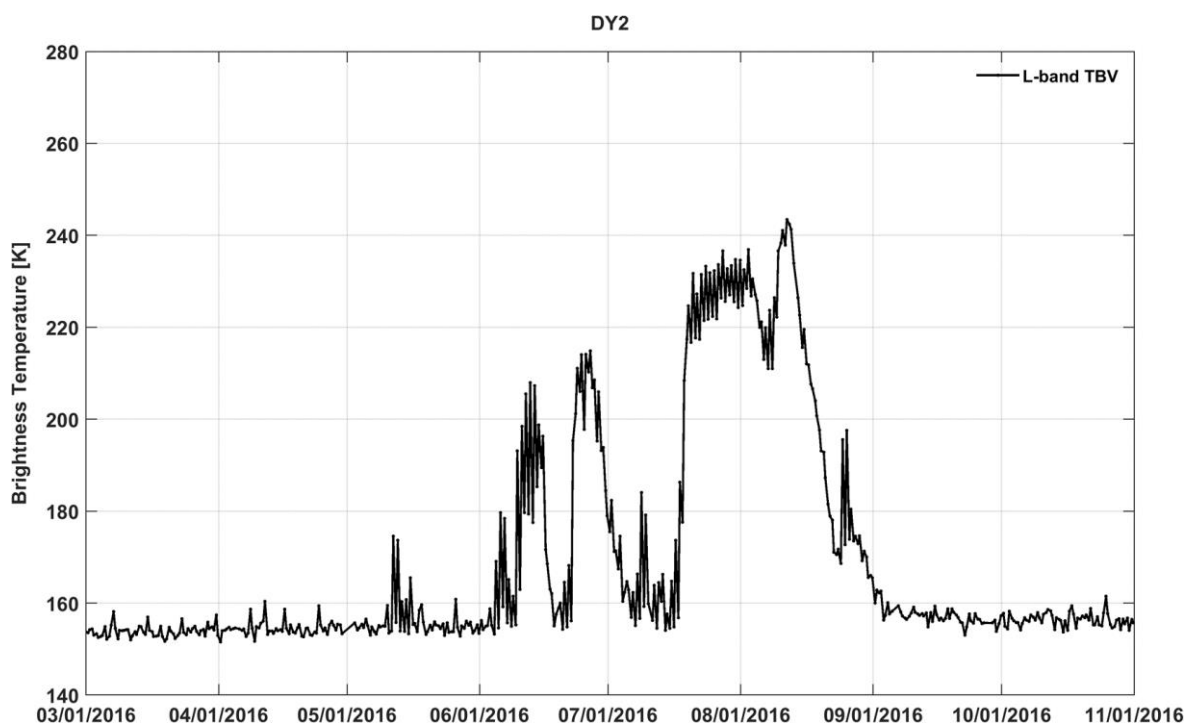
185

186 **Figure 2: Radiometric response of L- band TB during frozen and melt season. The location of K-transect is highlighted by red line**  
 187 **over the mean frozen season TBV map (a). Corresponding TBs across the transect are shown in (b): the black line represents the**  
 188 **mean V-pol TB during the frozen season (Jan 1 – Apr 7th of the same year). The red dash-dotted line indicates TB responses on a**  
 189 **sample melt day (Jul 31, 2019). The blue square symbols on the red dashed-dotted line depict melt flags (melt detections).**  
 190 **Approximate location of ablation, percolation, and upper accumulation zones are depicted along the K-transect for reference.**

191 Figure 3 shows the L-band V-pol TB time series during Mar – Oct 2016 at the DY2 AWS, a location representative  
 192 of the percolation zone. During the frozen season, the L-band TB is relatively lower and stable. During the melt season, it  
 193 captures the diurnal signals during melting phases (melt generation). However, it diminishes as the melt percolates to deeper  
 194 layers. From the onset through the end of the melt season, the density and grain size increase in the snow and firn layers due



195 to melt (Vandecrux et al., 2022). Although the L-band TB is relatively insensitive to the grain growth, the post-melt TB level  
 196 may still decrease because of increased reflection from newly formed ice layers. This effect is pervasive, especially across the  
 197 accumulation zone justifying a dynamic threshold in threshold-based melt detection algorithms.



198  
 199 **Figure 3: L- band V-pol TB time series at the DY2 automatic weather station location during during Mar – Oct, 2016 illustrating**  
 200 **the change of TB level caused by melting, snow accumulation, and other physical processes.**

### 201 2.3 Melt Retrieval Algorithm

202 We used a threshold-based empirical detection algorithm to detect surface and subsurface melt events. The threshold is  
 203 determined by:

$$204 T = \mu \pm m\sigma \quad (4)$$

205 where  $\mu$  is a reference TB (the mean during the frozen season),  $\sigma$  is the standard deviation of the TB during the reference  
 206 period, and  $m$  is an empirically derived constant. A constant value of 10 was chosen for  $m$ . First, to detect the first and last  
 207 melt during a year for a grid point, mean TB during Jan 1 – Apr 7<sup>th</sup>, and October 24 – December 31 was used as the reference  
 208 values, respectively. An averaged value of  $\sigma_{spring}$  and  $\sigma_{fall}$  is used with final adjustment of  $m$  in such a way that the threshold  
 209 does not miss the first and last melts. Then a linearly transitional reference value is used between the first and last melt days  
 210 to account for the change in TB value for subsequent melt because of refreezing.





211 We used an inversion of a simplified ice sheet emission model to estimate the LWA and physical properties of the  
212 detected melt events. The retrieval algorithm consists of a multi-layer forward model (Fig. 4) simulating the L-band TB  
213 (Mousavi et al., 2021) and a cost function minimization between the simulated and observed TB. The forward model represents  
214 the ice sheet as a stack of  $N+1$  vertical layers, where each layer is characterized by its complex dielectric constant ( $\epsilon$ ), density  
215 ( $\rho$ ), physical temperature ( $T$ ), and thickness ( $d$ ). The top and the bottom layers are assumed to be semi-infinite, while the  
216 intermediate layers are configured with variable thicknesses. The TB is then modelled using the incoherent approach of  
217 radiative transfer (RT) theory, without considering the effects of volume scattering analytically (but considering its dielectric  
218 effects explicitly). For a specific depth  $z$ , the upwelling TB, for a given polarization,  $p$ , is given by:

$$219 \quad T_{Bnp}^u(\theta_n, z) = [\Gamma_{np} T_{Bnp}^d(\theta_n, -d_n) + (1 - \Gamma_{np}) T_{B(n+1)p}^u(\theta_{(n+1)}, -d_n)] e^{-k_{an}(z+d_n) \sec \theta_n} + (1 - e^{-k_{an}(z+d_n) \sec \theta_n}) T_n$$

220 (5)

221 where  $T_{Bnp}^u$  and  $T_{Bnp}^d$  represents the upwelling and downwelling p-polarized TB at the interface  $z = -d_n$  characterized by  
222 reflectivity  $\Gamma_{np}$ .  $\theta_n$  is the incidence angle determined from the Snell's law and dielectric constant, and  $k_{an}$  is the power  
223 absorption coefficient given by  $k_{an} = -2\text{Re}\{\omega\sqrt{\epsilon_n\mu_0}\}$ , where  $\omega$  is the angular frequency,  $\epsilon_n$  is the complex permittivity of  
224 the layer, and  $\mu_0$  is the magnetic permeability for a nonmagnetic material.  $T_n$  is the physical temperature of the layer and  
225 assumed to be homogenous within the layer. The downwelling part of the TB,  $T_{Bnp}^d(\theta_n, -d_n)$ , is given by:

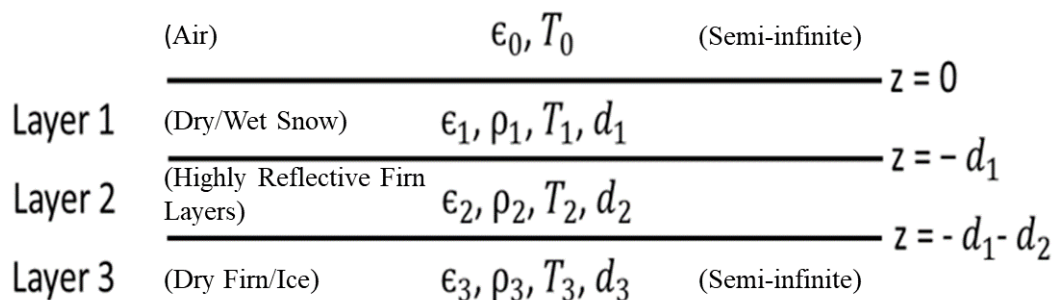
$$226 \quad T_{Bnp}^d(\theta_n, -d_n) = \Gamma_{(n-1)p} T_{Bnp}^u(\theta_n, -d_{n-1}) + (1 - \Gamma_{(n-1)p}) T_{B(n-1)p}^d(\theta_{(n-1)}, -d_{n-1})$$

227 (6)

228 It is assumed that there are no downward and upward emissions beyond the top ( $z = 0$ ) and bottom ( $z = -d_N$ ) semi-  
229 infinite layers respectively, and the atmospheric attenuation is also to be negligible considering L-band frequency. Therefore,  
230 the top-of-the atmosphere TB is found from equation (1),

$$230 \quad T_{BP}(\theta_0, H) \approx T_{B0p}^u(\theta_0, 0) = (1 - \Gamma_{0p}) T_{B1p}^u(\theta_1, 0)$$

231 (7)



231  
 232 **Figure 4: L-band multilayer ice sheet forward model.**

233 Following (Mousavi et al., 2021), the TB simulation considers the percolation zone of the GrIS as a four-layer medium (N=3)  
 234 during melt season -- air, a wet snow/firn layer, a highly reflective firn layer, and a semi-infinite firn/ice layer (Fig. 4). The  
 235 highly reflective layer represents the combined reflective effects by the complex stratigraphy due to numerous ice layers that  
 236 is present in the percolation zone of the GrIS, as well as the effects of volume scattering inside the same layer (Mousavi et al.,  
 237 2021). It is modeled as a layer of higher complex permittivity. For faster processing during retrieval, we developed separate  
 238 look-up-tables (LUTs) for dry and melt season prescribing layer parameters by sweeping over a realistic range of each  
 239 parameter. During dry season, the wet layer is absent (corresponding to dry snow layer that is assumed to be effectively  
 240 transparent when completely frozen) and the complex permittivity that best matches the measurements is prescribed to the  
 241 reflective layer.

242 The LUTs were revised compared to their original versions (Mousavi et al., 2021) in the following way. For each  
 243 layer, density (varying from a fresh snow density of 50 kg/m<sup>3</sup> to that of solid ice of 917 kg/m<sup>3</sup>) and physical temperature  
 244 (varying from 200 K to 273.15 K) were prescribed. The dielectric constant of the layers was calculated based on the density  
 245 and physical temperature following Ulaby and Long, 2014 and Mätzler, 2006. Then, the emission model was run for each  
 246 combination. The model computes the top-of-the-atmosphere L-band TB at the V- and H-pol based on frequency, incidence  
 247 angle, and the layers' thickness and dielectric constant. For the melt season, the wet snow layer is inserted with a volume  
 248 fraction of meltwater,  $m_w$ , which is varied from 0 to 5% in 40 equally spaced steps, and thickness,  $d_{wet}$ , which is varied from  
 249 10 cm to 20 m, in 10 cm steps for the top 60 cm, 20 cm steps for next 1.4 m, 40 cm steps for next 8 m, and 1 m steps for the



250 next 10 m. For  $m_v > 0$ ,  $T_{wet}$  must be 0 C. With all these constraints, the tuning finally results in two LUTs with six and eight  
251 dimensions for the dry and melt seasons, respectively.

252 The inversion was performed by optimizing a cost function that minimizes the distance between the LUT-modeled  
253 TB and the corresponding SMAP-measured TB for each 3.125 km grid cell. The optimization was carried out in two steps for  
254 each melting grid. First, the frozen season snow/firn density, physical temperature, and dielectric constant were estimated.  
255 Second, using that information, the volume fraction of meltwater  $m_v$ , and corresponding wet layer thickness  $d_{wet}$ , were  
256 determined for a time stamp during the melt season. The LWA is thus the product of the two, i.e.,  $LWA = m_v d_{wet}$  [m] m.w.e.  
257 This represents the instantaneous total LWA present in the SMAP footprint for that time stamp within the SMAP sensing  
258 depth, covering the typical infiltration of the meltwater in the percolation zone as per the climatological records (Samimi et  
259 al., 2020; Vandecrux et al., 2020). The detection algorithm uses both increasing and decreasing summer TBs to generate melt  
260 flags; however, the inversion only considered increasing TBs for LWA quantification. We averaged twice daily LWA outputs  
261 to compute daily samples.

## 262 **2.4 Automatic Weather Station Measurements**

263 Direct measurements of LWA are not available for validation. However, AWS networks, such as the Greenland Climate  
264 Network (GC-Net) (Steffen et al., 1996; Steffen and Box, 2001) or the Programme for Monitoring the Greenland Ice Sheet  
265 (PROMICE) (Fausto et al., 2021), provide essential surface parameters that can be used to estimate LWA with an energy  
266 balance model. The Geological Survey of Denmark and Greenland (GEUS), now manages these two AWS networks, which  
267 cumulate 33 active ice sheet sites in Greenland that provide a suite of measurements, such as incoming/outgoing short and  
268 longwave radiation fluxes, snow-surface height, air temperature, air pressure, vector winds, as well as subsurface temperature  
269 and density profiles (Fausto et al., 2021).

270 We used the hourly measurements from six PROMICE and GC-Net AWSs in the percolation zone to force an EMB  
271 model that produce a reference LWA, which was then used to validate the LWA retrieved from SMAP observations. The  
272 stations were selected considering their locations (see Fig. 5) and melt climatology. The meteorological forcing governs the  
273 surface energy budget (SEB) and was used to derive a coupled energy balance and snow/firn hydrology model (Ebrahimi and  
274 Marshall, 2016; Samimi et al., 2021) that provide an estimate of hourly LWC evolution within snow and firn.

## 275 **2.5 Ice Sheet Energy Balance and Hydrology Model**

276 The energy balance model (EBM) determines the net energy available for melt by considering the SEB along with modelled  
277 surface temperature, thermal emissivity, and albedo. The coupled model also accounts for the hydrological processes like  
278 meltwater infiltration, refreezing, and retention within the firn. We used two ice sheet EBMs for comparisons with the SMAP  
279 LWA retrievals. A detailed description of these models is out of the scope of this article, but brief descriptions are given below.  
280 Readers are referred to relevant cited articles for further details.



## 281 **2.5.1 Energy Balance and Hydrology Model**

282 A locally calibrated and validated EBM (Ebrahimi and Marshall, 2016; Samimi et al., 2020, 2021) was used as the primary  
283 reference for comparison. The EBM was initialized with ice core density profiles, stratigraphy, and the sub-surface temperature  
284 profiles (Vandecrux et al., 2023b) and forced with the hourly surface forcing from PROMICE and GC-Net AWS. The model  
285 first calculates the net energy balance from the surface forcing by combining the energy fluxes towards the surface layer. Then,  
286 it runs a subsurface model to calculate heat conduction and melt rates in the upper 20 m of the snow/finn by resolving the  
287 profile into 43 vertical layers, with gradually decreasing thickness near the surface.

288 When the surface temperature reaches the melting point, and the net energy is positive, melting occurs. Conversely,  
289 if net energy is negative and the surface layer is at the melting point, any existing liquid water will freeze, releasing latent heat  
290 and causing the surface layer to cool until all liquid water is refrozen, depending on the energy balance. When surface layer  
291 temperatures are below the melting point, and there is either an excess or deficit of energy leading to warming or cooling, the  
292 energy balance within a one-dimensional model of subsurface temperature evolution determines the subsurface temperature  
293 and density profiles. The model determines hydraulic conductivity and permeability after Meyer and Hewitt (2017), while  
294 thermal conductivity was modeled following Calonne et al., (2019). The profile then governs the availability of local water at  
295 any level for the next time stamp. The model relates to a basic approach to how meltwater flux percolates downward using  
296 Darcy's law. The local water balance is determined by mass conservation in each subsurface layer. Once a layer becomes  
297 temperate, it can retain liquid water within its pore space or allow it to percolate deeper (Coléou and Lesaffre, 1998). The  
298 subsurface model is coupled with a hydrology model that redistributes the meltwater; depending on the subsurface temperature  
299 profile, the meltwater may refreeze. Due to refreezing, density may increase, and ice layers may form that may reduce or  
300 completely block meltwater infiltration. The finn densification was modeled as in Vionnet et al., (2012). We henceforth refer  
301 to this model with AWS forcing as the EBM for simplicity. To evaluate the LWA retrieval, we calculate the daily average  
302 LWA from the hourly EBM output.

## 303 **2.5.2 Glacier Energy and Mass Balance (GEMB) Model**

304 We used output from GEMBv1.0 as a secondary source of comparison. It is a module in the Ice-sheet and Sea-level System  
305 Model (ISSM, <https://issm.jpl.nasa.gov/>) that models the ice sheet surface-energy and mass exchange and snow/finn state in a  
306 1D column over time (Gardner et al., 2023). It has more than 100 vertical layers with <5 cm thickness in the top layers and  
307 employs spatially variable grid size based on the ice sheet dynamics. GEMB formulates irreducible water content according  
308 to Colbeck, (1973), and uses bucket scheme (Steger et al., 2017) for liquid water infiltration. Parameterization of finn  
309 densification and thermal conductivity follow Herron and Langway, (1980) and Sturm et al., (1997) respectively. Readers are  
310 referred to Gardner et al., (2023) and references therein for further details. The model was forced with 3-hourly ERA5  
311 (Hersbach et al., 2020) atmosphere and radiation conditions, after the methods described by Paolo et al., (2023). For the GrIS  
312 output presented here, the ERA5 surface temperature and downwelling longwave radiation forcing were spatially bias-



313 corrected for each month, such that all values were adjusted by the difference between the RACMO2.3 (Noël et al., 2016) and  
314 the ERA5 1980-2015 monthly means. GEMB outputs were provided on the ISSM native grid, daily from 2015 through 2023  
315 and included temperature, density, and LWC profiles. The daily output of the closest grids to the selected AWSs was used.  
316 We henceforth refer to this model as GEMB.

### 317 **2.5.3 Evaluation Metrics**

318 To compare SMAP LWA time series with EBM and GEMB model, we considered the standard evaluation metrics including  
319 mean difference, standard deviation (STD), mean absolute difference (MAD), Pearson linear correlation coefficient ( $r$ ), root  
320 mean square error (RMSE). We also compared day of melt onset (the first day of summer melt) and melt freeze up (the last  
321 day of summer melt), summer melt duration (difference of melt onset and freeze up), maximum summer LWA, and annual  
322 sum of daily LWA ( $LWA_{YS}$ ). To determine the day of melt onset and freeze up, we only considered melt events with  $LWA >$   
323  $2$  mm, to avoid any spurious melts that may result from any instrumental noise or other sources. The  $LWA_{YS}$  is the sum of  
324 daily LWA over a year. It is a measure of the total seasonal LWA, but it does not represent the total surface melt generated  
325 over a year. This is because SMAP observes the instantaneous LWA, the net water balance, which is the cumulative sum of  
326 surface melt, refreezing, and runoff over SMAP footprint. When the net water balance remains positive overnight, it can be  
327 considered multiple times in the total integrated LWA as long as it persists.

## 328 **3 Results**

### 329 **3.1 Liquid Water Amount**

#### 330 **3.1.1 Comparison to Locally Calibrated EBM**

331 Figure 5 shows a comparison of the SMAP-retrieved LWA with the LWA derived from the EBM at six different PROMICE  
332 and GC-Net AWS sites for one year. The melt season at CP1 site (Figure 5a) began at the fourth week of June according to  
333 both, SMAP and the EBM, and continued through the first week of September according to SMAP, while it extended through  
334 the end of September in the model estimate. Shortly after complete refreezing of the first melt event in late June, SMAP  
335 resumed recording LWA in first week of July. Both SMAP and the EBM closely agree in both phase and magnitude of LWA  
336 during first half of July. Afterwards, the EBM reports overall higher LWA for the rest of the season and it seemed to retain  
337 liquid water for an elongated period when SMAP showed a fully refrozen firm. The overall agreement is given by the Pearson  
338 linear correlation coefficient ( $r$ ) of 0.82 and root mean square difference (RMSD) of 13 mm. The onset of melt event at KAN\_U  
339 site (Figure 5b) is concurrent to CP1 in accordance with the EBM. However, SMAP did not record melt at this site until the  
340 first week of July. Unlike CP1 site, SMAP reports persistent LWA through the first week of October, whereas EBM shows  
341 complete refreezing by the second week of September. Both SMAP and the EBM captured less LWA at KAN\_U site compared  
342 to CP1. This is somewhat counter-intuitive because the KAN\_U site is located at a lower elevation than CP1 site (see the

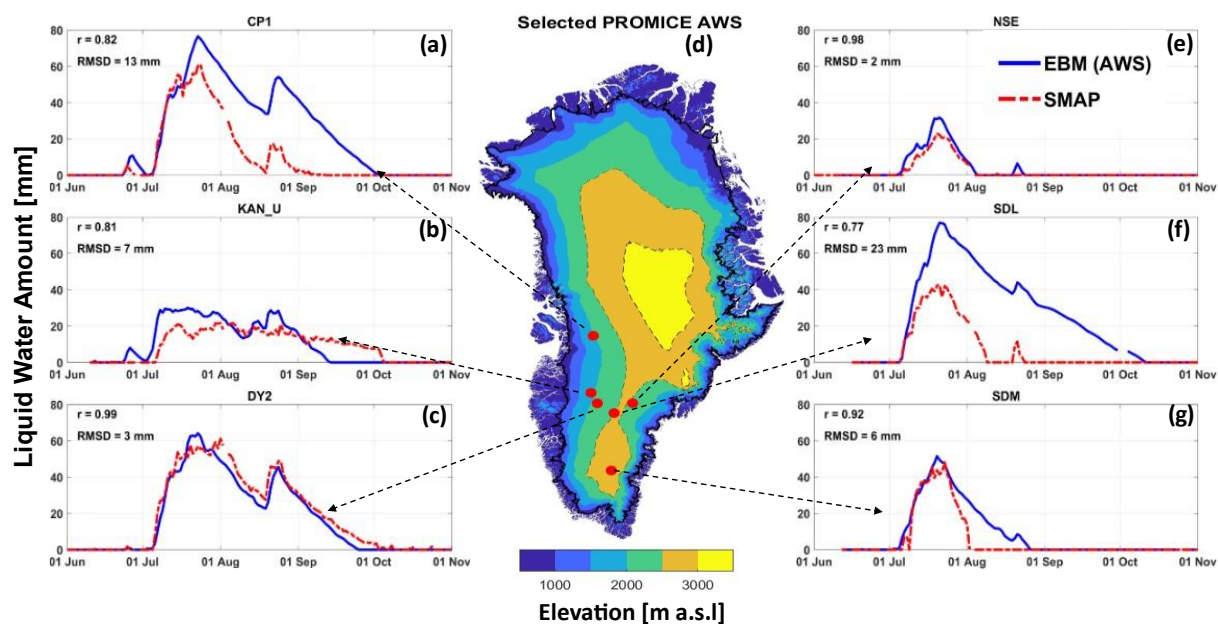


343 elevation in Figure 5d). In fact, KAN\_U is characterized by having a lower accumulation and higher melt rate every year  
344 (MacFerrin et al., 2019; Machguth et al., 2016). However, excessive melt have also created thick ice slabs in this location  
345 (MacFerrin et al., 2019; Machguth et al., 2016). As a result, liquid water cannot percolate to the deeper layers and run off  
346 horizontally. The model excludes this liquid water in the form of ‘drainage’, and SMAP only sees the existing meltwater in its  
347 field of view. At the DY2 site (Figure 5c), LWA estimated by SMAP, and the EBM resemble more closely both in phase and  
348 magnitude (except the difference in timing of complete freeze up). This is reflected by nearly perfect correlation and a small  
349 overall RMSD (3 mm) as shown.

350 SMAP LWA also closely aligns with the EBM at NSE site in magnitude and duration of liquid water presence ( $r =$   
351  $0.98$  and  $\text{RMSD} = 2$  mm) although SMAP seemed to miss the late August small melt event (Figure 5e). The agreement however  
352 exhibits the greatest deficiencies at SDL site for this melt season (Figure 5f). Although the timing of the melt onset and late  
353 August secondary melt event matches precisely, the EBM reports overall a higher LWA and an extended summer melt duration  
354 at this location. This is manifested in the performance metrics shown by a relatively higher RMSD (23 mm) and lower  
355 correlation coefficient (0.77). The performance at SDM site is generally good ( $r = 0.92$ , and  $\text{RMSD} = 6$  mm), except the EBM  
356 demonstrates a delayed refreezing than SMAP (Figure 5g).

357 It is pertinent to highlight that while *in situ* LWA at all these AWS were derived from the energy balance model  
358 forced by the pointwise measurements at the AWS locations, the SMAP retrievals estimated a spatially averaged LWA  
359 corresponding to the ~30 km effective resolution of the enhanced-resolution TB. Approximately, during the first half of the  
360 melt season, the LWA is primarily determined by meltwater generation in response to the net radiation flux at the surface.  
361 Whereas, roughly during the second half when the net radiation flux remains negative, refreezing becomes the dominant  
362 process. Hence, the model’s representation of the surface melt infiltration, heat transfer, and other physical processes play a  
363 significant role, posing additional uncertainties. The AWS measurements that run the model also add some inherent  
364 uncertainties. Therefore, assessing relative accuracies is not straightforward. Nevertheless, the general agreements between  
365 the model and SMAP retrieved LWA in magnitude and phase at these locations suggest that the spatial heterogeneity of melt  
366 processes is not acute in these areas.

367



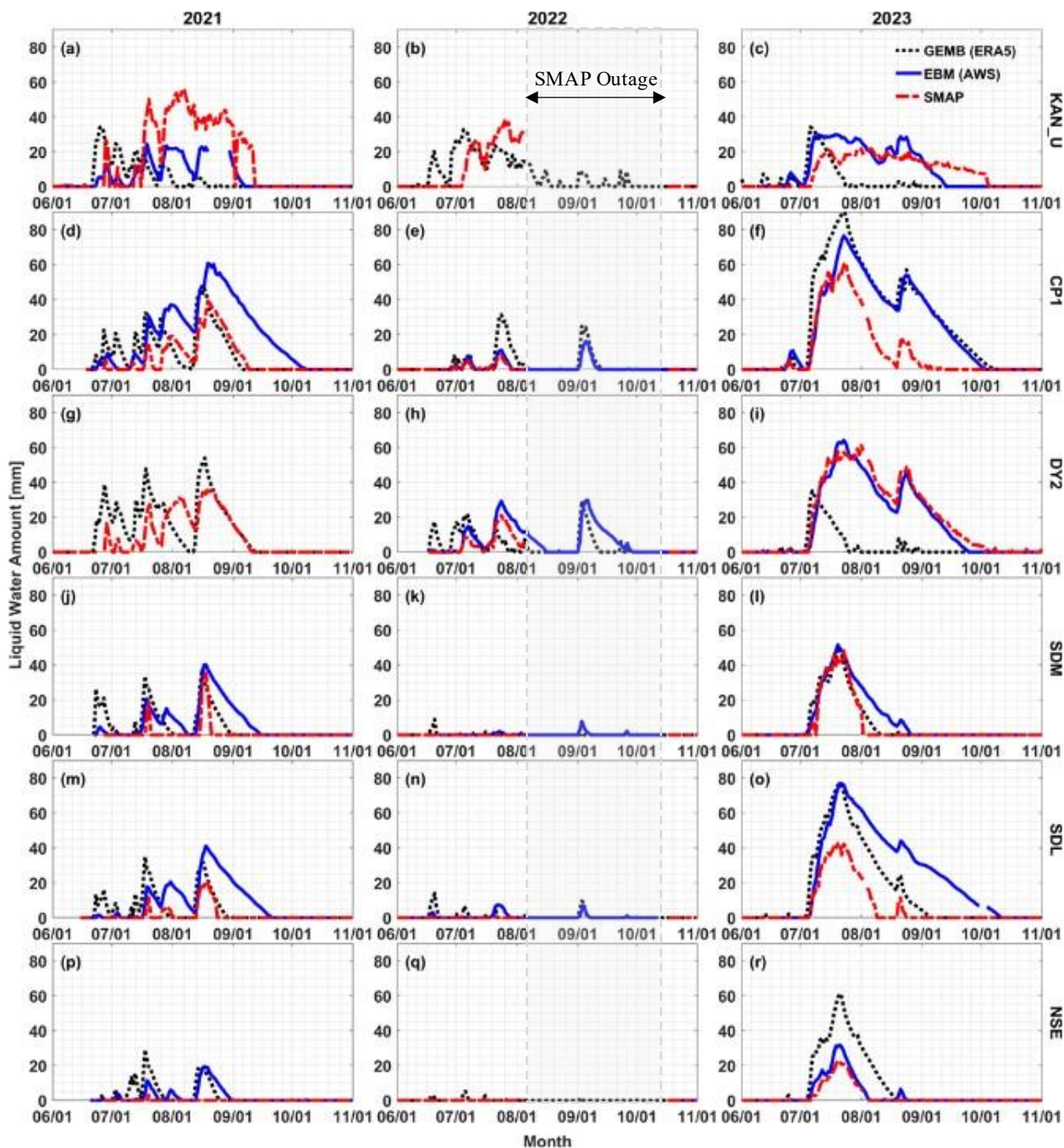
368

369 **Figure 5: Comparison of the total daily liquid water amount retrieved from SMAP (red dashed lines labeled SMAP) and estimated**  
 370 **by the EBM forced with *in situ* measurements (blue lines labeled EBM) at selected PROMICE and GC-Net AWS within the GrIS**  
 371 **percolation area. The locations of the AWSs are shown in the middle panel along with the ice sheet surface elevation (Howat et al.,**  
 372 **2014).**

373 **3.1.2 Three Way Comparison: SMAP, EBM, and GEMB Model**

374 We performed a pairwise comparison among SMAP, EBM, and GEMB models (Figure 6) for the 2021, 2022 and 2023 melt  
 375 seasons (based on available meteorological data) at the 6 AWS locations. In detail performance metrics are documented in  
 376 Table 1 (mean difference, STD, mean absolute difference, Pearson linear correlation coefficient, and RMSD) and Table 2  
 377 (melt onset, freeze up, duration of summer melt, maximum summer melt, and annual sum of daily LWA). Because of SMAP  
 378 outage for 2022 summer, performance metrics in Table 1 only considered the operational part of SMAP. Table 2, however,  
 379 excludes SMAP for 2022 melt season except the melt onset information as the other metrics were impacted by the outage.

380 At KAN\_U site, the overall agreement between SMAP and the EBM was determined to be better ( $r > 0.8$ ) than the  
 381 agreement either SMAP and GEMB model ( $r < 0.7$ ), or the EBM and GEMB model ( $r < 0.5$ ) for the 2021 and 2023 melt  
 382 seasons (Figure 6a-6c). All the AWS data required to run the EBM for 2022 melt season were not available. GEMB model  
 383 demonstrates earlier melt onset and freeze up and thus shortest summer melt duration in 2021 and 2023 melt seasons compared  
 384 to both SMAP and the EBM. SMAP estimated a maximum summer melt of 56 mm at this site in 2021 melt season, while both  
 385 the EBM and GEMB model recorded maximum summer melt of 34 mm in 2023 melt season. No pair shows consistent  
 386 superiority at CP1 site



387

388 **Figure 6: Comparison of the SMAP retrieved total daily liquid water amount (red dashed lines) with the estimated LWA from EBM**  
389 **(blue solid lines), and GEMB model (black dotted lines) at selected PROMICE and GC-Net AWS within the GrIS percolation area.**





390 (Figure 6d-6f). SMAP LWA generally aligns closer with GEMB model LWA in 2021 melt season, and with the EBM in 2022  
 391 melt season, whereas in 2023 melt season, the EBM and GEMB model matches closer to each other than to SMAP. DY2 lacks  
 392 AWS forcing during 2021 melt season. So, EBM result is missing for this melt season. Between SMAP and GEMB model,  
 393 the later estimates overall more LWA (LWA<sub>YS</sub> 1196 mm vs 1708 mm). There is a close alignment between the peaks of the  
 394 two LWA time series, one during the first week of August when SMAP reports about 30 mm LWA, while GEMB model  
 395 indicates no melt (Figure 6g). The overall RMSD was found to be 7.24 mm. For the other two melt seasons (Figure 6h-6i),  
 396 SMAP and the EBM results show superior agreements ( $r > 0.96$  and RMSD  $\sim 3$  mm). GEMB model reports significantly lower  
 397 LWA, both in magnitude and duration (only 564 mm LWA<sub>YS</sub> compared to 2893 mm (SMAP) and 2608 mm (EBM) resulting  
 398 in a higher overall RMSD ( $>15$  mm) with the other two.

399 **Table 1: Pairwise performance comparison among (a) SMAP, (b) EBM, and (c) GEMB models. Cells are left blank for**  
 400 **missing data.**

	Year	Mean Difference (mm)			Standard Deviation (STD) (mm)			Mean Absolute Difference (MAD) (mm)			Pearson Correlation Coefficient (r)			Root Mean Square Difference (RMSE) (mm)		
		a-b	a-c	b-c	a-b	a-c	b-c	a-b	a-c	b-c	a-b	a-c	b-c	a-b	a-c	b-c
AWS KAN_U	2021	-3.20	-4.70	0.25	8.94	14.31	6.22	3.53	6.34	2.37	0.89	0.20	0.36	9.48	15.04	6.22
	2022		0.17			5.98			2.08			0.71			5.98	
	2023	1.08	-2.60	5.07	6.72	7.58	9.48	4.55	4.10	5.90	0.81	0.26	0.49	6.79	8.00	10.73
CPI	2021	8.65	1.82	6.50	10.58	7.45	13.30	8.65	4.06	8.98	0.88	0.74	0.65	13.64	7.64	14.77
	2022	0.19	0.81	-1.08	0.71	3.49	3.58	0.24	0.82	1.12	0.97	0.87	0.87	0.74	3.58	3.73
	2023	5.82	7.50	-1.59	11.74	12.92	5.63	6.07	7.52	1.83	0.82	0.89	0.97	13.09	14.93	5.84
DY2	2021		1.26			7.17			2.73			0.75			7.27	
	2022	1.48	0.74	1.64	2.87	5.66	6.55	1.51	2.90	3.54	0.96	0.37	0.53	3.22	5.68	6.73
	2023	-1.03	-7.59	5.87	2.76	15.72	14.29	1.40	8.08	6.45	0.99	0.42	0.41	2.94	17.44	15.43
SDM	2021	3.75	2.43	1.02	7.19	5.87	6.51	3.78	2.56	3.46	0.61	0.63	0.70	8.09	6.34	6.57
	2022	0.09	0.08	0.14	0.31	0.64	0.73	0.09	0.08	0.19			0.31	0.32	0.64	0.75
	2023	2.56	0.32	1.58	5.34	2.37	4.29	2.70	0.62	2.10	0.92	0.97	0.94	5.91	2.38	4.56
SDL	2021	4.83	2.02	2.49	7.92	5.23	8.57	4.83	2.13	4.93	0.70	0.71	0.53	9.25	5.59	8.91
	2022	0.23	0.23	-0.10	1.03	1.32	1.46	0.23	0.23	0.35	0.70	0.30	0.44	1.05	1.34	1.46
	2023	15.73	3.87	6.03	16.46	8.81	10.95	15.76	3.87	7.76	0.77	0.95	0.88	22.73	9.61	12.48
NSE	2021	1.45	1.97	-0.52	3.85	5.04	3.77	1.46	1.98	1.54	0.16	0.27	0.66	4.10	5.40	3.79
	2022		0.07			0.47			0.07						0.48	
	2023	0.91	2.97	-3.65	2.24	8.20	8.05	0.91	2.97	3.76	0.98	0.94	0.94	2.41	8.70	8.82

401 As per maximum summer melt and LWA<sub>YS</sub>, SDL, SDM and NSE sites experienced the highest LWA in 2023 melt  
 402 season compared to the other two melt seasons under consideration (Figure 6j-6r). SMAP did not record any LWA in any of  
 403 these sites during 2022 melt season when EBM (except NSE where AWS data were not available), and GEMB models also



404 reported the least LWA in three melt seasons (Figure 6k, 6n, and 6q). In 2021 melt season, SMAP estimated overall lower  
 405 LWA and shorter summer melt duration than that of EBM and GEMB models in these sites. But the agreements between EBM  
 406 and GEMB models are in the same orders (see Table 1 and Table 2), with EBM exhibited delayed refreezing consistently.

407 **Table 2: Comparison of individual performances: (a) SMAP, (b) EBM, and (c) GEMB models. A threshold of 2 mm**  
 408 **LWA was considered to avoid any spurious melt event. Cells are left blank for missing data.**

AWS	Year	Melt Onset (DOY)			Melt Freeze up (DOY)			Summer Melt Duration (days)			Maximum Summer LWA (mm)			Annual Sum of Daily LWA (mm-year)		
		SMAP	EBM	GEMB	SMAP	EBM	GEMB	SMAP	EBM	GEMB	SMAP	EBM	GEMB	SMAP	EBM	GEMB
KAN_U	2021	179	175	173	254	248	229	76	74	57	56	24	34	2212	736	652
	2022	186		168			270			103			33			1004
	2023	188	176	163	277	254	240	90	79	78	22	30	34	1302	1504	459
CPI1	2021	179	175	173	251	277	247	73	103	75	39	61	47	842	2471	1191
	2022	181	181	180		252	254		72	75		16	31		175	435
	2023	175	176	175	246	273	277	72	98	103	61	76	91	1569	3458	4029
DY2	2021	179		173	251		252	73		80	35		54	1196		1708
	2022	185	185	169		270	269		86	101		30	29		838	513
	2023	187	187	151	313	265	242	127	79	92	61	64	35	2893	2608	465
SDM	2021	200	175	174	232	256	241	33	82	68	35	40	38	164	857	663
	2022		245	169		269	171		25	3		8	9		32	25
	2023	188	187	186	213	237	220	26	51	35	48	52	50	775	1202	890
SDL	2021	200	185	174	235	261	239	36	77	66	21	41	35	195	1096	607
	2022		169	169		248	248		80	80		7	14		68	95
	2023	187	187	176	235	282	246	49	96	71	43	77	77	919	3383	2196
NSE	2021	201	185	177	201	241	235	1	57	59	3	19	29	5	271	371
	2022			171			197			27			5			21
	2023	188	187	176	214	234	232	27	48	57	23	32	61	338	508	1314

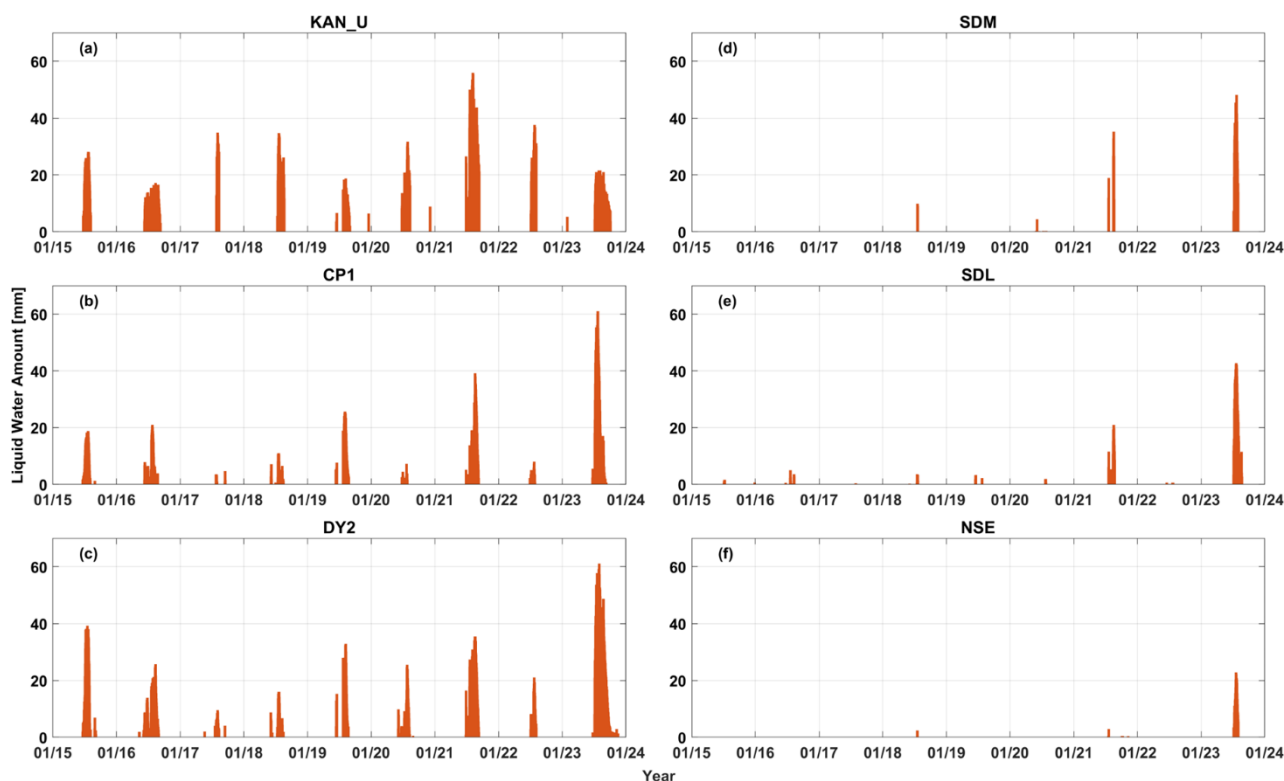
409

### 410 3.1.3 SMAP LWA Time Series

411 Figure 7 shows the SMAP retrieved LWA time series at the mentioned six AWS locations on the southwest and southeast  
 412 sides of the GrIS percolation zone. The time series do not include results during 2019 and 2022 outage. As evidenced, the  
 413 AWS sites in the southwest sites (Figure 7a-7c) experienced more average LWA and longer summer melt duration than the  
 414 AWS sites in southeast sites (Figure 7d-7f). SDL, SDM, and NSE witnessed an insignificant LWA (<10 mm) during 2015 -  
 415 2020 melt seasons. However, it was found to be increasing in recent years (Figure 7d-7f). SMAP recorded the highest LWA



416 in 2023 melt season during 2025 - 2023 at all the AWS locations, except at KAN\_U where 2021 marked the highest melt  
 417 season.  
 418



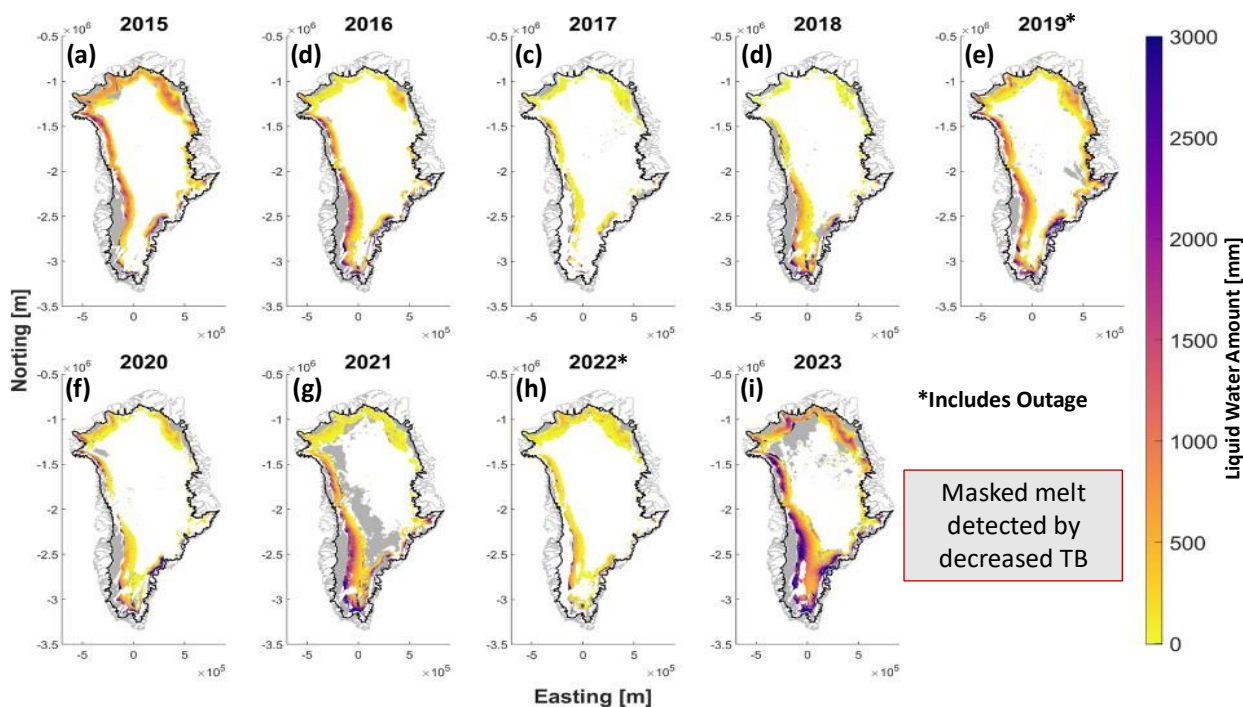
419  
 420 **Figure 7: SMAP retrieved LWA time series for 2015-2023 period at at six selected PROMICE and GC-Net AWS within the GrIS**  
 421 **percolation area.**

422 **3.1.4 Spatial Variability**

423 Figure 8 illustrates the annual sum of daily LWA ( $LWA_{YS}$ ) for 2015 – 2023. Here, we masked the area where melt is detected  
 424 by decreasing summer TBs (compared to winter reference). As mentioned in Sec. 2.2.3, current LWA quantification algorithm  
 425 applies to increasing TBs only. This excluded the melt flags in the ablation zone and upper accumulation zone as indicated by  
 426 grey shades in Figure 8. There were also some occasions when summer TB decreases below the winter threshold in the  
 427 percolation too. Those anomalies were probably caused by short lived melt events that refroze between SMAP passes and  
 428 impacted TBs. These anomalies are also masked and not included in the results. As depicted, SMAP captured the similar  
 429 spatial trends of LWA distribution across the percolation zone of GrIS as reported by previous studies (Van Den Broeke et al.,  
 430 2016; Houtz et al., 2021). In the time frame under consideration, 2023 melt season (Figure 8i) had the highest  $LWA_{YS}$  (2634  
 431 mm on average for the percolation area) while 2017 (Figure 8c) had the lowest value (757 mm on average for the percolation  
 432 area). In 2015 (Figure 8a), the northern ice sheet exhibited a relatively high  $LWA_{YS}$ ; similar intensity and extent were also



433 recorded for 2023 (Figure 8i). Notably, the melt extended to upper elevations in the dry snow zone in 2021 and 2023.  
 434 Unfortunately, SMAP outages in 2019 (Figure 8e) and 2022 (Figure 8h), lead to incomplete coverage for those years and lower  
 435 LWA<sub>YS</sub>. It is worthwhile to reiterate that the integrated LWA is a measure of the total seasonal LWA in the specified area.  
 436



437  
 438 **Figure 8: Total annual sum of SMAP daily LWA for 2015 - 2023. The black solid line represents GrIS edges, and the grey color**  
 439 **masks inside the ice sheet indicate melt detections by decreasing TB, which were not quantified.**

#### 440 4 Discussion

441 The L-band radiometry has the unique advantage of receiving the emission from the deep layers of ice sheets, offering the  
 442 opportunity to track meltwater from deeper layers. We have demonstrated its capability to estimate the seasonal LWA that  
 443 generally agrees with two state-of-the-art ice sheet models, one locally calibrated and forced with independent *in situ* AWS  
 444 measurements and the other forced with ERA5 reanalysis. The legitimacy of spatial and temporal variability shown in SMAP  
 445 retrieval for the percolation area of the GrIS is promising.

446 There are some disagreements as well, but those do not necessarily indicate a deficiency of the SMAP retrievals since  
 447 both the references are models with their own limitations. The differences between model results and SMAP retrievals are not  
 448 systematic, so they are difficult to explain; but there is no evidence of a consistent bias. Nonetheless, some of the discrepancies  
 449 between these estimations of LWA stem from the scale at which those datasets operate. The SMAP LWA was estimated from  
 450 the TB measurements averaged over a large footprint and a short integration time. Further, rSIR enhanced-resolution data



451 products involve overlapping observations to produce the 3.125 km gridded data but still has an effective spatial resolution of  
452 ~30 km. Thus, it represents near-instantaneous vertically integrated LWA, averaged over the grid point, whereas the AWS  
453 data is the hourly average of ‘point’ measurements representative of the 0.1-1 km surrounding the station. The total LWA from  
454 AWS-forced data is the hourly-averaged, vertically integrated net water balance which is determined as the cumulative sum  
455 of hourly surface melt generation, refreezing, and drainage. The surface melt generation is driven by the net surface energy  
456 balance (net radiation and turbulent heat fluxes), which involves uncertainties (e.g., the surface albedo and roughness; errors  
457 in the meteorological inputs), while how the melt and heat are distributed in subsurface firn involves additional uncertainties,  
458 including sensitivity to initial conditions (e.g., the firn temperature and density profile; Samimi et al., 2020). These models  
459 transform surface meteorological information into an amount of surface melt relying on loosely constrained parameterizations  
460 (Covi et al., 2023). Eventually, the models’ formulation for the meltwater infiltration is still poorly constrained (e.g. Vandecrux  
461 et al., 2020). Additionally, both the models we used (like other state-of-the-art firn models) are one dimensional – they only  
462 consider vertical movement of water and heat and do not account for horizontal advection. However, firn hydrological  
463 processes are complex and heterogeneous, and processes such as ice layer formation are intrinsically three-dimensional. What  
464 the models consider as ‘drainage’ (meltwater that moves out of the system) both vertically and horizontally could still be within  
465 the SMAP sensing depth and horizontal footprints. Hence, the comparison should be considered accordingly.

466 One important disagreement between SMAP and EBM LWA estimation, especially during the refreezing periods, is  
467 that EBM retained LWA for an extended period when SMAP showed complete refrozen condition (Figure 6). We used SUMup  
468 subsurface temperature measurements (Vandecrux et al., 2023b) to verify the cases for which SUMup data are available. One  
469 example is shown in Figure 9. It compares the model-estimated subsurface temperature (Figure 9a) corresponding to the 2021  
470 LWA at CP1 (Figure 6d) to the *in situ* measured subsurface temperature (Figure 9b). It is evident that although the penetration  
471 depth of the model wetting front closely matches the observation, the measurement demonstrates a higher and faster refreezing  
472 compared to the model. The subsurface measurement shows a fully refrozen condition by early September (closely agreeing  
473 with what was revealed by SMAP, see Figure 6d). However, the model seems to retain the subsurface meltwater with a  
474 persistent wetting front even past the beginning of October, which seems unlikely. Speculating extra melt production due to  
475 possible error in the AWS surface forcing, and other surface processes in the EBM, we examined modelled subsurface  
476 temperature profile by reducing surface melt with different factors ( $<1$ ). We also performed similar analysis with irreducible  
477 water content, thermal conductivity. In either case (not shown), we could not match the subsurface profile with measured  
478 profile within reasonable agreements. This incites questions regarding the model representation of meltwater infiltration, heat  
479 transfer, and refreezing.

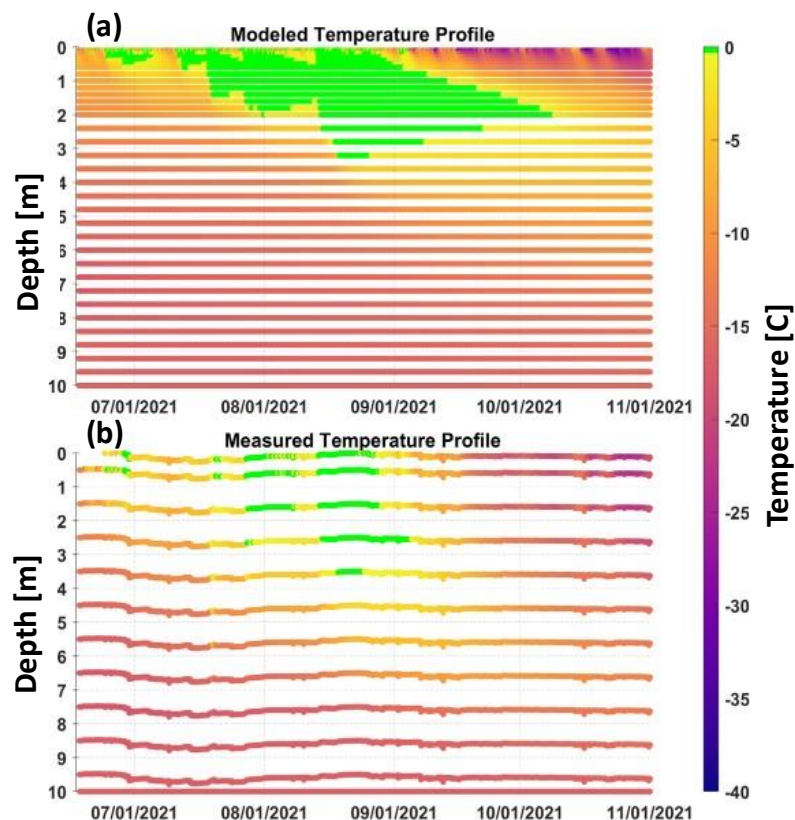
480 The models do not include meltwater infiltration by finger flow (piping). Some recent studies have shown that this is  
481 an important mechanism for moving liquid water from the surface to deep depths (e.g., Vandecrux et al, 2020). The piping  
482 events are short-lived penetration and refreezing events. SMAP will measure the LWC in the piping event, even when it passes  
483 the wetting front, unless the water is refrozen before the SMAP measurement (as is the case with all short-lived melt events).  
484 The model would calculate a certain amount of meltwater based on the surface energy balance, and it would put all this water



485 into the wetting front layer. However, from the literature and as confirmed by the subsurface temperature measurements (Figure  
486 9b), some fraction of this water would be partitioned into deep piping. The model only includes top-down migration of a  
487 wetting front. This may explain why there are discrepancies between the modelled subsurface temperature profile and the  
488 observed subsurface temperature profile in some cases. Indeed, the deep penetration events causing warming spikes beyond  
489 the wetting front distort the temperature profiles. Therefore, some differences between SMAP and the EBM and GEMB model  
490 could be attributed to this weakness in process representation in the model. But overall, these problems are multifaceted and  
491 additional works are required to understand the basis for these discrepancies. Yet, to this day, there is no observational dataset  
492 that allows to evaluate directly the LWA amount retrieved from satellite observations or calculated by a snow and firn model.

493 Besides the coarser spatial resolution, SMAP algorithm has its own shortcomings. The emission model simulated  
494 TBs with a simplified view of the stratigraphy which lacks detailed representation of snow and firn microstructures. The model  
495 also neglected atmospheric contributions and assumed homogenous medium and smooth surface within each layer. Although  
496 these effects are not significant at L-band, a detailed characterization was not done. Among other limitations, the detection  
497 algorithm follows a threshold-based technique that uses winter reference of the TB to detect melt events. As a result, it is  
498 capable quantifying the seasonal LWA only, not the LWA in perennial firn aquifers which stores a large quantity of the LWA  
499 on the GrIS (Miller et al., 2022a, b). Current algorithm also excluded areas where TB decreases during summer melt. Future  
500 work will be continued to overcome these limitations and refine the algorithm.

501 To extend the algorithm for GrIS-wide LWA quantification, the ablation zone presents a major challenge. Although  
502 SMAP can detect melt events in the ablation zone, the quantification is difficult for several reasons. The hydrological features  
503 of the ablation zone are markedly different from the percolation or upper accumulation zone. There are widespread networks  
504 of many supraglacial lakes and rivers, crevasses, and other complex heterogeneous factors, such as surface topography, dust  
505 deposition, slush saturation, etc. (Cooper and Smith, 2019; Poinar and C. Andrews, 2021; Smith et al., 2017). This generates  
506 an intricate radiometric response. The average LWA in ablation zone is also significantly higher limiting the L-band emission  
507 in the upper layer only. Houtz et al., (2019) used L-band observations from SMOS satellite to derive LWA at the Swiss Camp  
508 GC-Net AWS located in the ablation zone with a simplistic assumption of fixed (10 cm) wet layer thickness. More *in situ*  
509 observations are needed to characterize the spatial and temporal variability of LWA in the ablation zone.



510

511 **Figure 9: Modeled (a) and measured (b) subsurface temperatures corresponding to total LWA at CP1 site during 2021 melt season.**  
512 **The 0°C isotherm is highlighted by green color.**

## 513 5 Conclusion

514 we have demonstrated quantification of the total surface and subsurface meltwater amount over the Greenland ice sheet using  
515 the L-band radiometric observations from the SMAP mission. The retrieval algorithm was described, and the validation results  
516 with six *in situ* weather station measurements and reanalysis data were provided. The comparison results were analysed,  
517 showing that the retrieval generally agrees with the AWS-driven LWA across the percolation zone. The model uncertainties  
518 in representing firm hydrological and thermal processes were explored, and the greatest differences involve the timescale for  
519 internal refreezing. The model results commonly predict a longer season for liquid water content in the snow and near-surface  
520 firm, i.e., delays in refreezing relative to the SMAP data. Limitations of the SAMP and model estimates LWA, and possible  
521 reasons for the discrepancies between them were discussed. Further work is required to understand the basis for these  
522 discrepancies. The results demonstrate the potential for providing an observational dataset at time and space scales that will  
523 advance our understanding of ice sheet physical processes, helping to better project Greenland's contribution to global sea  
524 level rise in response to climate change and variability.



525

526 **Data and code availability**

527 SMAP Radiometer Twice-Daily rSIR-Enhanced EASE-Grid 2.0 Brightness Temperatures, Version 2 data products  
528 were provided by National Snow and Ice Data Center and are publicly available at <https://nsidc.org/data/nsidc-0738/versions/2>.  
529 The PROMICE hourly AWS measurements are available at <https://doi.org/10.22008/FK2/IW73UU> (How et al., 2022). The  
530 2023 version of the SUMup subsurface temperature and density profiles are available at  
531 <https://arcticdata.io/catalog/view/doi:10.18739/A2M61BR5M>. SMAP and model LWA are available in a Zenodo repository  
532 at <https://doi.org/10.5281/zenodo.13800047>. The scripts used to perform the analysis for this study can be found at  
533 [https://github.com/HossanAlamgir/SMAP\\_MWA\\_Retrieval\\_and\\_Validation\\_GrIS](https://github.com/HossanAlamgir/SMAP_MWA_Retrieval_and_Validation_GrIS). MATLAB source code for glacier surface  
534 energy balance coupled with firm thermodynamic and hydrological modelling is available in PRISM Data: University of  
535 Calgary's Data Repository at <https://doi.org/10.5683/SP2/WRWJAZ> (Marshall, 2021).

536 **Author contributions**

537 AH and AC designed the study and the methodology. AH performed the formal analysis and visualization. NS run the GEMB  
538 model and provided the outputs. AH and AC prepared the first draft of the paper. All the authors discussed the results and  
539 reviewed the paper. AC supervised the project and managed funding.

540 **Competing interests**

541 The authors declare that they have no conflicts of interest.

542 **Acknowledgements**

543 This work was funded by the NASA Cryospheric Sciences Program; the work was conducted at the Jet Propulsion  
544 Laboratory, California Institute of Technology, under a contract with the National Aeronautics and Space Administration. We  
545 gratefully acknowledge computational resources and support from the NASA Advanced Supercomputing Division. The  
546 Greenland maps were generated with the assistance of the Arctic Mapping Tools (Greene et al., 2017).

547 **References**

548 Abdalati, W. and Steffen, K.: Passive microwave-derived snow melt regions on the Greenland Ice Sheet, *Geophys. Res. Lett.*,  
549 22, 787–790, <https://doi.org/10.1029/95GL00433>, 1995.





- 550 Abdalati, W. and Steffen, K.: Snowmelt on the Greenland ice sheet as derived from passive microwave satellite data, *J. Clim.*,  
551 10, 165–175, [https://doi.org/10.1175/1520-0442\(1997\)010<0165:SOTGIS>2.0.CO;2](https://doi.org/10.1175/1520-0442(1997)010<0165:SOTGIS>2.0.CO;2), 1997.
- 552 Abdalati, W. and Steffen, K.: Greenland Ice Sheet melt extent: 1979–1999, *J. Geophys. Res. Atmos.*, 106, 33983–33988,  
553 <https://doi.org/https://doi.org/10.1029/2001JD900181>, 2001.
- 554 Ashcraft, I. and Long, D.: Comparison of methods for melt detection over greenland using active and passive Microwave  
555 measurements, *Int. J. Remote Sens.*, 27, 2469–2488, <https://doi.org/10.1080/01431160500534465>, 2006.
- 556 Brodzik, M. J., Long, D. G., and Hardman, M. A.: SMAP Twice-Daily rSIR-Enhanced, 1–51, 2021.
- 557 Van Den Broeke, M. R., Enderlin, E. M., Howat, I. M., Kuipers Munneke, P., Noël, B. P. Y., Jan Van De Berg, W., Van  
558 Meijgaard, E., and Wouters, B.: On the recent contribution of the Greenland ice sheet to sea level change, *Cryosphere*, 10,  
559 1933–1946, <https://doi.org/10.5194/tc-10-1933-2016>, 2016.
- 560 Calonne, N., Milliancourt, L., Burr, A., Philip, A., Martin, C. L., Flin, F., and Geindreau, C.: Thermal Conductivity of Snow,  
561 Firn, and Porous Ice From 3-D Image-Based Computations, *Geophys. Res. Lett.*, 46, 13079–13089,  
562 <https://doi.org/10.1029/2019GL085228>, 2019.
- 563 Chaubell, J., Yueh, S., Peng, J., Dunbar, S., Chan, S., Chen, F., Piepmeier, J., Bindlish, R., Entekhabi, D., and O’Neill, P.: Soil  
564 Moisture Active Passive (SMAP) Algorithm Theoretical Basis Document: SMAP L1(B/C) Enhanced Radiometer Brightness  
565 Temperature Data Product, 1, 1–32, 2018.
- 566 Chaubell, M. J., Chan, S., Dunbar, R. S., Peng, J., and Yueh, S.: SMAP Enhanced L1C Radiometer Half-Orbit 9 km EASE-  
567 Grid Brightness Temperatures, Version 1., 2020.
- 568 Christian Mätzler: Microwave dielectric properties of ice, *Transportation (Amst.)*, 1, 21–30,  
569 <https://doi.org/10.1002/ejoc.201200111>, 2006.
- 570 Citterio, M. and Ahlstrøm, A. P.: Brief communication the aerophotogrammetric map of Greenland ice masses, *Cryosphere*,  
571 7, 445–449, <https://doi.org/10.5194/tc-7-445-2013>, 2013.
- 572 Colbeck, S. C.: Theory of Metamorphism of Wet Snow., *US Army Corps Eng Cold Reg Res Eng Lab Res Rep*, 88, 5475–  
573 5482, 1973.
- 574 Coléou, C. and Lesaffre, B.: Irreducible water saturation in snow: experimental results in a cold laboratory, *Ann. Glaciol.*, 26,  
575 64–68, <https://doi.org/10.3189/1998aog26-1-64-68>, 1998.
- 576 Colliander, A., Mousavi, M., Misra, S., Brown, S., Kimball, J. S., Miller, J., Johnson, J., and Burgin, M.: Ice Sheet Melt Water  
577 Profile Mapping Using Multi-Frequency Microwave Radiometry, *Int. Geosci. Remote Sens. Symp.*, 2022-July, 4178–4181,  
578 <https://doi.org/10.1109/IGARSS46834.2022.9883717>, 2022a.
- 579 Colliander, A., Mousavi, M., Marshall, S., Samimi, S., Kimball, J. S., Miller, J. Z., Johnson, J., and Burgin, M.: Ice Sheet  
580 Surface and Subsurface Melt Water Discrimination Using Multi-Frequency Microwave Radiometry, *Geophys. Res. Lett.*, 49,  
581 <https://doi.org/10.1029/2021GL096599>, 2022b.
- 582 Colliander, A., Mousavi, M., Kimball, J. S., Miller, J. Z., and Burgin, M.: Spatial and temporal differences in surface and  
583 subsurface meltwater distribution over Greenland ice sheet using multi-frequency passive microwave observations, *Remote*



- 584 Sens. Environ., 295, 113705, <https://doi.org/10.1016/j.rse.2023.113705>, 2023.
- 585 Colosio, P., Tedesco, M., Ranzi, R., and Fettweis, X.: Surface melting over the Greenland ice sheet derived from enhanced  
586 resolution passive microwave brightness temperatures (1979-2019), *Cryosphere*, 15, 2623–2646, [https://doi.org/10.5194/tc-](https://doi.org/10.5194/tc-15-2623-2021)  
587 15-2623-2021, 2021.
- 588 Cooper, M. G. and Smith, L. C.: Satellite remote sensing of the Greenland Ice Sheet Ablation Zone: A review, *Remote Sens.*,  
589 11, 17–21, <https://doi.org/10.3390/rs11202405>, 2019.
- 590 Covi, F., Hock, R., and Reijmer, C. H.: Challenges in modeling the energy balance and melt in the percolation zone of the  
591 Greenland ice sheet, *J. Glaciol.*, 69, 164–178, <https://doi.org/10.1017/jog.2022.54>, 2023.
- 592 Culberg, R., Schroeder, D. M., and Chu, W.: Extreme melt season ice layers reduce firn permeability across Greenland, *Nat.*  
593 *Commun.*, 12, 1–9, <https://doi.org/10.1038/s41467-021-22656-5>, 2021.
- 594 Ebrahimi, S. and Marshall, S. J.: Surface energy balance sensitivity to meteorological variability on Haig Glacier, Canadian  
595 Rocky Mountains, *Cryosphere*, 10, 2799–2819, <https://doi.org/10.5194/tc-10-2799-2016>, 2016.
- 596 Elachi, C., and Van Zyl, J. J.: Introduction to the Physics and Techniques of Remote Sensing, John Wiley & Sons, 159–189  
597 pp., [https://doi.org/https://doi.org/10.1002/9781119523048.ch5](https://doi.org/10.1002/9781119523048.ch5), 2021.
- 598 Entekhabi, D., Njoku, E. G., O’Neill, P. E., Kellogg, K. H., Crow, W. T., Edelstein, W. N., Entin, J. K., Goodman, S. D.,  
599 Jackson, T. J., Johnson, J., Kimball, J., Piepmeier, J. R., Koster, R. D., Martin, N., McDonald, K. C., Moghaddam, M., Moran,  
600 S., Reichle, R., Shi, J. C., Spencer, M. W., Thurman, S. W., Tsang, L., and Van Zyl, J.: The soil moisture active passive  
601 (SMAP) mission, *Proc. IEEE*, 98, 704–716, <https://doi.org/10.1109/JPROC.2010.2043918>, 2010.
- 602 Fausto, R. S., Van As, D., Mankoff, K. D., Vandecrux, B., Citterio, M., Ahlstrøm, A. P., Andersen, S. B., Colgan, W., Karlsson,  
603 N. B., Kjeldsen, K. K., Korsgaard, N. J., Larsen, S. H., Nielsen, S., Pedersen, A., Shields, C. L., Solgaard, A. M., and Box, J.  
604 E.: Programme for Monitoring of the Greenland Ice Sheet (PROMICE) automatic weather station data, *Earth Syst. Sci. Data*,  
605 13, 3819–3845, <https://doi.org/10.5194/essd-13-3819-2021>, 2021.
- 606 Fettweis, X., van Ypersele, J. P., Gallée, H., Lefebvre, F., and Lefebvre, W.: The 1979-2005 Greenland ice sheet melt extent  
607 from passive microwave data using an improved version of the melt retrieval XPGR algorithm, *Geophys. Res. Lett.*, 34,  
608 <https://doi.org/10.1029/2006GL028787>, 2007.
- 609 Fettweis, X., Tedesco, M., Van Den Broeke, M., and Ettema, J.: Melting trends over the Greenland ice sheet (1958-2009) from  
610 spaceborne microwave data and regional climate models, *Cryosphere*, 5, 359–375, <https://doi.org/10.5194/tc-5-359-2011>,  
611 2011.
- 612 Fettweis, X., Hofer, S., Krebs-Kanzow, U., Amory, C., Aoki, T., Berends, C. J., Born, A., Box, J. E., Delhasse, A., Fujita, K.,  
613 Gierz, P., Goelzer, H., Hanna, E., Hashimoto, A., Huybrechts, P., Kapsch, M. L., King, M. D., Kittel, C., Lang, C., Langen, P.  
614 L., Lenaerts, J. T. M., Liston, G. E., Lohmann, G., Mernild, S. H., Mikolajewicz, U., Modali, K., Mottram, R. H., Niwano, M.,  
615 Noël, B., Ryan, J. C., Smith, A., Streffing, J., Tedesco, M., Jan Van De Berg, W., Van Den Broeke, M., Van De Wal, R. S.  
616 W., Van Kampenhout, L., Wilton, D., Wouters, B., Ziemen, F., and Zolles, T.: GrSMBMIP: Intercomparison of the modelled  
617 1980-2012 surface mass balance over the Greenland Ice Sheet, *Cryosphere*, 14, 3935–3958, [26](https://doi.org/10.5194/tc-14-</a></p></div><div data-bbox=)



- 618 3935-2020, 2020.
- 619 Gardner, A. S., Schlegel, N. J., and Larour, E.: Glacier Energy and Mass Balance (GEMB): A model of firm processes for  
620 cryosphere research, *Geosci. Model Dev.*, 16, 2277–2302, <https://doi.org/10.5194/gmd-16-2277-2023>, 2023.
- 621 Greene, C. A., Gwyther, D. E., and Blankenship, D. D.: Antarctic Mapping Tools for MATLAB, *Comput. Geosci.*, 104, 151–  
622 157, <https://doi.org/10.1016/j.cageo.2016.08.003>, 2017.
- 623 Greene, C. A., Gardner, A. S., Wood, M., and Cuzzone, J. K.: Ubiquitous acceleration in Greenland Ice Sheet calving from  
624 1985 to 2022, 625, <https://doi.org/10.1038/s41586-023-06863-2>, 2024.
- 625 Hall, D. K., Nghiem, S. V., Schaaf, C. B., DiGirolamo, N. E., and Neumann, G.: Evaluation of surface and near-surface melt  
626 characteristics on the Greenland ice sheet using MODIS and QuikSCAT data, *J. Geophys. Res. Earth Surf.*, 114, 1–13,  
627 <https://doi.org/10.1029/2009JF001287>, 2009.
- 628 Harper, J., Humphrey, N., Pfeffer, W. T., Brown, J., and Fettweis, X.: Greenland ice-sheet contribution to sea-level rise  
629 buffered by meltwater storage in firn, *Nature*, 491, 240–243, <https://doi.org/10.1038/nature11566>, 2012.
- 630 Heilig, A., Eisen, O., MacFerrin, M., Tedesco, M., and Fettweis, X.: Seasonal monitoring of melt and accumulation within the  
631 deep percolation zone of the Greenland Ice Sheet and comparison with simulations of regional climate modeling, *Cryosphere*,  
632 12, 1851–1866, <https://doi.org/10.5194/tc-12-1851-2018>, 2018.
- 633 Herron MM and Langway CC: Firn densification: an empirical model. *Journal of Glaciology* 25(93), 373–385. doi:, 25, 1980.
- 634 Hersbach, H., Bell, B., Berrisford, P., Hirahara, S., Horányi, A., Muñoz-Sabater, J., Nicolas, J., Peubey, C., Radu, R., Schepers,  
635 D., Simmons, A., Soci, C., Abdalla, S., Abellan, X., Balsamo, G., Bechtold, P., Biavati, G., Bidlot, J., Bonavita, M., De Chiara,  
636 G., Dahlgren, P., Dee, D., Diamantakis, M., Dragani, R., Flemming, J., Forbes, R., Fuentes, M., Geer, A., Haimberger, L.,  
637 Healy, S., Hogan, R. J., Hólm, E., Janisková, M., Keeley, S., Laloyaux, P., Lopez, P., Lupu, C., Radnoti, G., de Rosnay, P.,  
638 Rozum, I., Vamborg, F., Villaume, S., and Thépaut, J. N.: The ERA5 global reanalysis, *Q. J. R. Meteorol. Soc.*, 146, 1999–  
639 2049, <https://doi.org/10.1002/qj.3803>, 2020.
- 640 Hoffman, M. J., Catania, G. A., Neumann, T. A., Andrews, L. C., and Rumrill, J. A.: Links between acceleration, melting, and  
641 supraglacial lake drainage of the western Greenland Ice Sheet, *J. Geophys. Res. Earth Surf.*, 116, 1–16,  
642 <https://doi.org/10.1029/2010JF001934>, 2011.
- 643 Houtz, D., Naderpour, R., Schwank, M., and Steffen, K.: Snow wetness and density retrieved from L-band satellite radiometer  
644 observations over a site in the West Greenland ablation zone, *Remote Sens. Environ.*, 235, 111361,  
645 <https://doi.org/10.1016/j.rse.2019.111361>, 2019.
- 646 Houtz, D., Mätzler, C., Naderpour, R., Schwank, M., and Steffen, K.: Quantifying Surface Melt and Liquid Water on the  
647 Greenland Ice Sheet using L-band Radiometry, *Remote Sens. Environ.*, 256, <https://doi.org/10.1016/j.rse.2021.112341>, 2021.
- 648 How, P., Abermann, J., Ahlstrøm, A. P., Andersen, S. B., Box, J. E., Citterio, M., Colgan, W. T., R.S., F., Karlsson, N. B.,  
649 Jakobsen, J., Langley, K., Larsen, S. H., Lund, M. C., Mankoff, K. D., Pedersen, A. Ø., Rutishauser, A., Shield, C. L., Solgaard,  
650 A. M., van As, D., Vandecrux, B., and Wright, P. J.: PROMICE and GC-Net automated weather station data in Greenland,  
651 <https://doi.org/doi:10.22008/FK2/IW73UU>, 2022.



- 652 Jay Zwally, H.: Microwave Emissivity and Accumulation Rate of Polar Firn, *J. Glaciol.*, 18, 195–215,  
653 <https://doi.org/10.3189/s0022143000021304>, 1977.
- 654 Jezek, K. C., Johnson, J. T., Tan, S., Tsang, L., Andrews, M. J., Brogioni, M., MacElloni, G., Durand, M., Chen, C. C.,  
655 Belgiovane, D. J., Duan, Y., Yardim, C., Li, H., Bringer, A., Leuski, V., and Aksoy, M.: 500-2000-MHz Brightness  
656 Temperature Spectra of the Northwestern Greenland Ice Sheet, *IEEE Trans. Geosci. Remote Sens.*, 56, 1485–1496,  
657 <https://doi.org/10.1109/TGRS.2017.2764381>, 2018.
- 658 Jin, Y.-Q.: Electromagnetic Scattering Modelling for Quantitative Remote Sensing, *WORLD SCIENTIFIC*, 348 pp.,  
659 <https://doi.org/doi:10.1142/2253>, 1994.
- 660 Jin, Y.: Radiative transfer theory at satellite-borne SSM/I channels and remote sensing data analysis, *Sci. China, Ser. E*  
661 *Technol. Sci.*, 40, 644–652, <https://doi.org/10.1007/bf02916850>, 1997.
- 662 Jullien, N., Tedstone, A. J., Machguth, H., Karlsson, N. B., and Helm, V.: Greenland Ice Sheet Ice Slab Expansion and  
663 Thickening, *Geophys. Res. Lett.*, 50, 1–9, <https://doi.org/10.1029/2022GL100911>, 2023.
- 664 Khan, S. A., Aschwanden, A., Björk, A. A., Wahr, J., Kjeldsen, K. K., and Kjaær, K. H.: Greenland ice sheet mass balance:  
665 A review, *Reports Prog. Phys.*, 78, <https://doi.org/10.1088/0034-4885/78/4/046801>, 2015.
- 666 Khan, S. A., Bamber, J. L., Rignot, E., Helm, V., Aschwanden, A., Holland, D. M., van den Broeke, M., King, M., Noël, B.,  
667 Truffer, M., Humbert, A., Colgan, W., Vijay, S., and Kuipers Munneke, P.: Greenland Mass Trends From Airborne and  
668 Satellite Altimetry During 2011–2020, *J. Geophys. Res. Earth Surf.*, 127, 1–20, <https://doi.org/10.1029/2021JF006505>, 2022.
- 669 Long, D. G., Brodzik, M. J., and Hardman, M. A.: Enhanced-Resolution SMAP Brightness Temperature Image Products, *IEEE*  
670 *Trans. Geosci. Remote Sens.*, 57, 4151–4163, <https://doi.org/10.1109/TGRS.2018.2889427>, 2019.
- 671 Long, D. G., Brodzik, M. J., and Hardman, M.: Evaluating the effective resolution of enhanced resolution SMAP brightness  
672 temperature image products, *Front. Remote Sens.*, 4, 1–10, <https://doi.org/10.3389/frsen.2023.1073765>, 2023.
- 673 MacFerrin, M., Machguth, H., As, D. van, Charalampidis, C., Stevens, C. M., Heilig, A., Vandecrux, B., Langen, P. L.,  
674 Mottram, R., Fettweis, X., Broeke, M. R. van den, Pfeffer, W. T., Moussavi, M. S., and Abdalati, W.: Rapid expansion of  
675 Greenland’s low-permeability ice slabs, *Nature*, 573, 403–407, <https://doi.org/10.1038/s41586-019-1550-3>, 2019.
- 676 Machguth, H., Macferrin, M., Van As, D., Box, J. E., Charalampidis, C., Colgan, W., Fausto, R. S., Meijer, H. A. J., Mosley-  
677 Thompson, E., and Van De Wal, R. S. W.: Greenland meltwater storage in firn limited by near-surface ice formation, *Nat.*  
678 *Clim. Chang.*, 6, 390–393, <https://doi.org/10.1038/nclimate2899>, 2016.
- 679 Marshall, S. J.: MATLAB code for firn thermodynamic and hydrological modeling, 2021.
- 680 Medley, B., Neumann, T. A., Zwally, H. J., Smith, B. E., and Stevens, C. M.: Simulations of firn processes over the Greenland  
681 and Antarctic ice sheets: 1980-2021, *Cryosphere*, 16, 3971–4011, <https://doi.org/10.5194/tc-16-3971-2022>, 2022.
- 682 Meyer, C. R. and Hewitt, I. J.: A continuum model for meltwater flow through compacting snow, *Cryosphere*, 11, 2799–2813,  
683 <https://doi.org/10.5194/tc-11-2799-2017>, 2017.
- 684 Mikkelsen, A. B., Hubbard, A., Macferrin, M., Eric Box, J., Doyle, S. H., Fitzpatrick, A., Hasholt, B., Bailey, H. L., Lindbäck,  
685 K., and Pettersson, R.: Extraordinary runoff from the Greenland ice sheet in 2012 amplified by hypsometry and depleted firn



- 686 retention, *Cryosphere*, 10, 1147–1159, <https://doi.org/10.5194/tc-10-1147-2016>, 2016.
- 687 Miller, J. Z., Long, D. G., Jezek, K. C., Johnson, J. T., Brodzik, M. J., Shuman, C. A., Koenig, L. S., and Scambos, T. A.: Brief  
688 communication: Mapping Greenland’s perennial firn aquifers using enhanced-resolution L-band brightness temperature image  
689 time series, *Cryosphere*, 14, 2809–2817, <https://doi.org/10.5194/tc-14-2809-2020>, 2020a.
- 690 Miller, J. Z., Culberg, R., Long, D. G., Shuman, C. A., Schroeder, D. M., and Brodzik, M. J.: An empirical algorithm to map  
691 perennial firn aquifers and ice slabs within the Greenland Ice Sheet using satellite L-band microwave radiometry, *Cryosphere*,  
692 16, 103–125, <https://doi.org/10.5194/tc-16-103-2022>, 2022a.
- 693 Miller, J. Z., Long, D. G., Shuman, C. A., Culberg, R., Hardman, M., and Brodzik, M. J.: Mapping Firn Saturation Over  
694 Greenland Using NASA’s Soil Moisture Active Passive Satellite, *IEEE J. Sel. Top. Appl. Earth Obs. Remote Sens.*, 15, 3714–  
695 3729, <https://doi.org/10.1109/JSTARS.2022.3154968>, 2022b.
- 696 Miller, O., Solomon, D. K., Miège, C., Koenig, L., Forster, R., Schmerr, N., Ligtenberg, S. R. M., Legchenko, A., Voss, C. I.,  
697 Montgomery, L., and McConnell, J. R.: Hydrology of a Perennial Firn Aquifer in Southeast Greenland: An Overview Driven  
698 by Field Data, *Water Resour. Res.*, 56, <https://doi.org/10.1029/2019WR026348>, 2020b.
- 699 Mote, T. L.: Greenland surface melt trends 1973–2007: Evidence of a large increase in 2007, *Geophys. Res. Lett.*, 34, 1–5,  
700 <https://doi.org/10.1029/2007GL031976>, 2007.
- 701 Mote, T. L. and Anderson, M. R.: Variations in snowpack melt on the Greenland ice sheet based on passive-microwave  
702 measurements, *J. Glaciol.*, 41, 51–60, <https://doi.org/10.1017/S0022143000017755>, 1995.
- 703 Mouginit, J., Rignot, E., Bjørk, A. A., van den Broeke, M., Millan, R., Morlighem, M., Noël, B., Scheuchl, B., and Wood,  
704 M.: Forty-six years of Greenland Ice Sheet mass balance from 1972 to 2018, *Proc. Natl. Acad. Sci. U. S. A.*, 116, 9239–9244,  
705 <https://doi.org/10.1073/pnas.1904242116>, 2019.
- 706 Mousavi, M., Colliander, A., Miller, J. Z., Entekhabi, D., Johnson, J. T., Shuman, C. A., Kimball, J. S., and Courville, Z. R.:  
707 Evaluation of Surface Melt on the Greenland Ice Sheet Using SMAP L-Band Microwave Radiometry, *IEEE J. Sel. Top. Appl.*  
708 *Earth Obs. Remote Sens.*, 14, 11439–11449, <https://doi.org/10.1109/JSTARS.2021.3124229>, 2021.
- 709 Mousavi, M., Colliander, A., Miller, J., and Kimball, J. S.: A Novel Approach to Map the Intensity of Surface Melting on the  
710 Antarctica Ice Sheet Using SMAP L-Band Microwave Radiometry, *IEEE J. Sel. Top. Appl. Earth Obs. Remote Sens.*, 15,  
711 1724–1743, <https://doi.org/10.1109/JSTARS.2022.3147430>, 2022.
- 712 Nghiem, S. V., Steffen, K., Kwok, R., and Tsai, W. Y.: Detection of snowmelt regions on the Greenland ice sheet using diurnal  
713 backscatter change, *J. Glaciol.*, 47, 539–547, <https://doi.org/10.3189/172756501781831738>, 2001.
- 714 Noël, B., Jan Van De Berg, W., MacHuth, H., Lhermitte, S., Howat, I., Fettweis, X., and Van Den Broeke, M. R.: A daily, 1  
715 km resolution data set of downscaled Greenland ice sheet surface mass balance (1958–2015), *Cryosphere*, 10, 2361–2377,  
716 <https://doi.org/10.5194/tc-10-2361-2016>, 2016.
- 717 Otosaka, I. N., Shepherd, A., Ivins, E. R., Schlegel, N. J., Amory, C., Van Den Broeke, M. R., Horwath, M., Joughin, I., King,  
718 M. D., Krinner, G., Nowicki, S., Payne, A. J., Rignot, E., Scambos, T., Simon, K. M., Smith, B. E., Sørensen, L. S., Velicogna,  
719 I., Whitehouse, P. L., Geruo, A., Agosta, C., Ahlstrøm, A. P., Blazquez, A., Colgan, W., Engdahl, M. E., Fettweis, X., Forsberg,



- 720 R., Gallée, H., Gardner, A., Gilbert, L., Gourmelen, N., Groh, A., Gunter, B. C., Harig, C., Helm, V., Khan, S. A., Kittel, C.,  
721 Konrad, H., Langen, P. L., Lecavalier, B. S., Liang, C. C., Loomis, B. D., McMillan, M., Melini, D., Mernild, S. H., Mottram,  
722 R., Mouginot, J., Nilsson, J., Noël, B., Pattle, M. E., Peltier, W. R., Pie, N., Roca, M., Sasgen, I., Save, H. V., Seo, K. W.,  
723 Scheuchl, B., Schrama, E. J. O., Schröder, L., Simonsen, S. B., Slater, T., Spada, G., Sutterley, T. C., Vishwakarma, B. D.,  
724 Van Wessem, J. M., Wiese, D., Van Der Wal, W., and Wouters, B.: Mass balance of the Greenland and Antarctic ice sheets  
725 from 1992 to 2020, *Earth Syst. Sci. Data*, 15, 1597–1616, <https://doi.org/10.5194/essd-15-1597-2023>, 2023.
- 726 Paolo, F. S., Gardner, A. S., Greene, C. A., Nilsson, J., Schodlok, M. P., Schlegel, N. J., and Fricker, H. A.: Widespread  
727 slowdown in thinning rates of West Antarctic ice shelves, *Cryosphere*, 17, 3409–3433, [https://doi.org/10.5194/tc-17-3409-](https://doi.org/10.5194/tc-17-3409-2023)  
728 2023, 2023.
- 729 Picard, G., Brucker, L., Roy, A., Dupont, F., Fily, M., Royer, A., and Harlow, C.: Simulation of the microwave emission of  
730 multi-layered snowpacks using the Dense Media Radiative transfer theory: the DMRT-ML model, *Geosci. Model Dev.*, 6,  
731 1061–1078, <https://doi.org/10.5194/gmd-6-1061-2013>, 2013.
- 732 Picard, G., Leduc-Leballeur, M., Banwell, A. F., Brucker, L., and Macelloni, G.: The sensitivity of satellite microwave  
733 observations to liquid water in the Antarctic snowpack, *Cryosphere*, 16, 5061–5083, <https://doi.org/10.5194/tc-16-5061-2022>,  
734 2022.
- 735 Piepmeier, J. R., Focardi, P., Horgan, K. A., Knuble, J., Ehsan, N., Lucey, J., Brambora, C., Brown, P. R., Hoffman, P. J.,  
736 French, R. T., Mikhaylov, R. L., Kwack, E. Y., Slimko, E. M., Dawson, D. E., Hudson, D., Peng, J., Mohammed, P. N., De  
737 Amici, G., Freedman, A. P., Medeiros, J., Sacks, F., Estep, R., Spencer, M. W., Chen, C. W., Wheeler, K. B., Edelstein, W.  
738 N., O’Neill, P. E., and Njoku, E. G.: SMAP L-Band Microwave Radiometer: Instrument Design and First Year on Orbit, *IEEE*  
739 *Trans. Geosci. Remote Sens.*, 55, 1954–1966, <https://doi.org/10.1109/TGRS.2016.2631978>, 2017.
- 740 Poinar, K. and C. Andrews, L.: Challenges in predicting Greenland supraglacial lake drainages at the regional scale,  
741 *Cryosphere*, 15, 1455–1483, <https://doi.org/10.5194/tc-15-1455-2021>, 2021.
- 742 Samimi, S., Marshall, S. J., and MacFerrin, M.: Meltwater Penetration Through Temperate Ice Layers in the Percolation Zone  
743 at DYE-2, Greenland Ice Sheet, *Geophys. Res. Lett.*, 47, 1–9, <https://doi.org/10.1029/2020GL089211>, 2020.
- 744 Samimi, S., Marshall, S. J., Vandecrux, B., and MacFerrin, M.: Time-Domain Reflectometry Measurements and Modeling of  
745 Firn Meltwater Infiltration at DYE-2, Greenland, *J. Geophys. Res. Earth Surf.*, 126, <https://doi.org/10.1029/2021JF006295>,  
746 2021.
- 747 Schoof, C.: Ice-sheet acceleration driven by melt supply variability, *Nature*, 468, 803–806,  
748 <https://doi.org/10.1038/nature09618>, 2010.
- 749 Schwank, M. and Naderpour, R.: Snow density and ground permittivity retrieved from L-band radiometry: Melting effects,  
750 *Remote Sens.*, 10, 1–26, <https://doi.org/10.3390/rs10020354>, 2018.
- 751 Shepherd, A., Ivins, E., Rignot, E., Smith, B., van den Broeke, M., Velicogna, I., Whitehouse, P., Briggs, K., Joughin, I.,  
752 Krinner, G., Nowicki, S., Payne, T., Scambos, T., Schlegel, N., A. G., Agosta, C., Ahlstrøm, A., Babonis, G., Barletta, V. R.,  
753 Bjørk, A. A., Blazquez, A., Bonin, J., Colgan, W., Csatho, B., Cullather, R., Engdahl, M. E., Felikson, D., Fettweis, X.,



- 754 Forsberg, R., Hogg, A. E., Gallee, H., Gardner, A., Gilbert, L., Gourmelen, N., Groh, A., Gunter, B., Hanna, E., Harig, C.,  
755 Helm, V., Horvath, A., Horwath, M., Khan, S., Kjeldsen, K. K., Konrad, H., Langen, P. L., Lecavalier, B., Loomis, B., Luthcke,  
756 S., McMillan, M., Melini, D., Mernild, S., Mohajerani, Y., Moore, P., Mottram, R., Mouginot, J., Moyano, G., Muir, A.,  
757 Nagler, T., Nield, G., Nilsson, J., Noël, B., Otosaka, I., Pattle, M. E., Peltier, W. R., Pie, N., Rietbroek, R., Rott, H.,  
758 Sandberg Sørensen, L., Sasgen, I., Save, H., Scheuchl, B., Schrama, E., Schröder, L., Seo, K. W., Simonsen, S. B., Slater, T.,  
759 Spada, G., Sutterley, T., Talpe, M., Tarasov, L., van de Berg, W. J., van der Wal, W., van Wessem, M., Vishwakarma, B. D.,  
760 Wiese, D., Wilton, D., Wagner, T., Wouters, B., and Wuite, J.: Mass balance of the Greenland Ice Sheet from 1992 to 2018,  
761 *Nature*, 579, 233–239, <https://doi.org/10.1038/s41586-019-1855-2>, 2020.
- 762 Smith, L. C., Yang, K., Pitcher, L. H., Overstreet, B. T., Chu, V. W., Rennermalm, Å. K., Ryan, J. C., Cooper, M. G., Gleason,  
763 C. J., Tedesco, M., Jeyaratnam, J., Van As, D., Van Den Broeke, M. R., Van De Berg, W. J., Noël, B., Langen, P. L., Cullather,  
764 R. I., Zhao, B., Willis, M. J., Hubbard, A., Box, J. E., Jenner, B. A., and Behar, A. E.: Direct measurements of meltwater runoff  
765 on the Greenland ice sheet surface, *Proc. Natl. Acad. Sci. U. S. A.*, 114, E10622–E10631,  
766 <https://doi.org/10.1073/pnas.1707743114>, 2017.
- 767 Steffen, K. and Box, J. E.: Surface climatology of the Greenland ice sheet : Overview of study area . Monthly mean sea level  
768 pressure fields for ( b ) January , November the National Centers for Environmental Prediction, *J. Geophys. Res.*, 106, 33951–  
769 33964, 2001.
- 770 Steffen, K., Box, J. E., and Abdalati, W.: Greenland climate network: GC-Net, US Army Cold Reg. Reatt. Eng. (CRREL),  
771 CRREL Spec. Rep., 98–103, 1996.
- 772 Steger, C. R., Reijmer, C. H., and Van Den Broeke, M. R.: The modelled liquid water balance of the Greenland Ice Sheet,  
773 *Cryosphere*, 11, 2507–2526, <https://doi.org/10.5194/tc-11-2507-2017>, 2017.
- 774 Sturm, M., Holmgren, J., König, M., and Morris, K.: The thermal conductivity of seasonal snow, *J. Glaciol.*, 43, 26–41,  
775 <https://doi.org/10.1017/S0022143000002781>, 1997.
- 776 Sundal, A. V., Shepherd, A., Nienow, P., Hanna, E., Palmer, S., and Huybrechts, P.: Melt-induced speed-up of Greenland ice  
777 sheet offset by efficient subglacial drainage, *Nature*, 469, 521–524, <https://doi.org/10.1038/nature09740>, 2011.
- 778 Tedesco, M.: Snowmelt detection over the Greenland ice sheet from SSM/I brightness temperature daily variations, *Geophys.*  
779 *Res. Lett.*, 34, 1–6, <https://doi.org/10.1029/2006GL028466>, 2007.
- 780 Tedesco, M.: Assessment and development of snowmelt retrieval algorithms over Antarctica from K-band spaceborne  
781 brightness temperature (1979–2008), *Remote Sens. Environ.*, 113, 979–997, <https://doi.org/10.1016/j.rse.2009.01.009>, 2009.
- 782 Tedesco, M., Abdalati, W., and Zwally, H. J.: Persistent surface snowmelt over Antarctica (1987–2006) from 19.35 GHz  
783 brightness temperatures, *Geophys. Res. Lett.*, 34, 1–6, <https://doi.org/10.1029/2007GL031199>, 2007.
- 784 Tedstone, A. J. and Machguth, H.: Increasing surface runoff from Greenland’s firm areas, *Nat. Clim. Chang.*, 12, 672–676,  
785 <https://doi.org/10.1038/s41558-022-01371-z>, 2022.
- 786 Thompson-Munson, M., Wever, N., Stevens, C. M., Lenaerts, J. T. M., and Medley, B.: An evaluation of a physics-based firm  
787 model and a semi-empirical firm model across the Greenland Ice Sheet (1980–2020), *Cryosphere*, 17, 2185–2209,



- 788 <https://doi.org/10.5194/tc-17-2185-2023>, 2023.
- 789 Tsang, L., Chen, C.-T., Chang, A. T. C., Guo, J., and Ding, K.-H.: Dense media radiative transfer theory based on  
790 quasicrystalline approximation with applications to passive microwave remote sensing of snow, *Radio Sci.*, 35, 731–749,  
791 <https://doi.org/10.1029/1999RS002270>, 2000.
- 792 Ulaby, F. and Long, D.: Microwave Radar and Radiometric Remote Sensing, *Microw. Radar Radiom. Remote Sens.*,  
793 <https://doi.org/10.3998/0472119356>, 2014.
- 794 Vandecrux, B., MacFerrin, M., MacHguth, H., Colgan, W. T., Van As, D., Heilig, A., Max Stevens, C., Charalampidis, C.,  
795 Fausto, R. S., Morris, E. M., Mosley-Thompson, E., Koenig, L., Montgomery, L. N., Miège, C., Simonsen, S. B., Ingeman-  
796 Nielsen, T., and Box, J. E.: Firn data compilation reveals widespread decrease of firn air content in western Greenland,  
797 *Cryosphere*, 13, 845–859, <https://doi.org/10.5194/tc-13-845-2019>, 2019.
- 798 Vandecrux, B., Mottram, R., L. Langen, P., S. Fausto, R., Olesen, M., Max Stevens, C., Verjans, V., Leeson, A., Ligtenberg,  
799 S., Kuipers Munneke, P., Marchenko, S., Van Pelt, W., R. Meyer, C., B. Simonsen, S., Heilig, A., Samimi, S., Marshall, S.,  
800 MacHguth, H., MacFerrin, M., Niwano, M., Miller, O., I. Voss, C., and E. Box, J.: The firn meltwater Retention Model  
801 Intercomparison Project (RetMIP): Evaluation of nine firn models at four weather station sites on the Greenland ice sheet,  
802 *Cryosphere*, 14, 3785–3810, <https://doi.org/10.5194/tc-14-3785-2020>, 2020.
- 803 Vandecrux, B., Box, J. E., Wehrlé, A., Kokhanovsky, A. A., Picard, G., Niwano, M., Hörhold, M., Faber, A. K., and Steen-  
804 Larsen, H. C.: The Determination of the Snow Optical Grain Diameter and Snowmelt Area on the Greenland Ice Sheet Using  
805 Spaceborne Optical Observations, *Remote Sens.*, 14, <https://doi.org/10.3390/rs14040932>, 2022.
- 806 Vandecrux, B., Fausto, R. S., Box, J. E., Covi, F., Hock, R., Rennermalm, A. K., Heilig, A., Abermann, J., Van As, D., Bjerre,  
807 E., Fettweis, X., Smeets, P. C. J. P., Kuipers Munneke, P., Van Den Broeke, M. R., Brils, M., Langen, P. L., Mottram, R., and  
808 Ahlstrøm, A. P.: Historical snow and ice temperature observations document the recent warming of the Greenland ice sheet,  
809 1985, 609–631, 2023a.
- 810 Vandecrux, B., Amory, C., Ahlstrøm, A. P., Akers, P. D., Albert, M., Alley, B., Arnaud, L., Bales, R., Benson, C., Box, J. E.,  
811 Buizert, C., Charalampidis, C., Clerx, N., Covi, F., Denis, G., Dibb, J. E., Ding, M., Eisen, O., Fausto, R., Fernandoy, F.,  
812 Freitag, J., Niwano, M., Osterberg, E., Otosaka, I., Picard, G., and Rennermalm, A.: The SUMup collaborative database :  
813 Surface mass balance , subsurface temperature and density measurements from the Greenland and Antarctic ice sheets, 1–58  
814 pp., 2023b.
- 815 Verjans, V., Leeson, A. A., Max Stevens, C., MacFerrin, M., Noël, B., and Van Den Broeke, M. R.: Development of physically  
816 based liquid water schemes for Greenland firn-densification models, *Cryosphere*, 13, 1819–1842, <https://doi.org/10.5194/tc-13-1819-2019>, 2019.
- 817 Vionnet, V., Brun, E., Morin, S., Boone, A., Faroux, S., Le Moigne, P., Martin, E., and Willemet, J. M.: The detailed snowpack  
818 scheme Crocus and its implementation in SURFEX v7.2, *Geosci. Model Dev.*, 5, 773–791, <https://doi.org/10.5194/gmd-5-773-2012>, 2012.
- 820 Wismann, V.: Monitoring of seasonal snowmelt on Greenland with ERS scatterometer data, *IEEE Trans. Geosci. Remote*





- 822 Sens., 38, 1821–1826, <https://doi.org/10.1109/36.851766>, 2000.
- 823 Zwally, H. J. and Fiegles, S.: Extent and duration of Antarctic surface melting, *J. Glaciol.*, 40, 463–476,  
824 <https://doi.org/10.3189/s0022143000012338>, 1994.
- 825 Zwally, H. J., Abdalati, W., Herring, T., Larson, K., Saba, J., and Steffen, K.: Surface Melt – Induced Acceleration of  
826 Greenland Ice-Sheet Flow, 297, 218–222, 2002.
- 827